ACS APPLIED ENERGY MATERIALS

Multiphase-Field Simulation Studies of Coarsening in Ni-GDC SOFC Anode Microstructures and the Effect of Interfacial Energies

R. K. Jeela,* M. Ahmad, M. Wieler, Y. Liu, M. Juckel, D. Schneider,* A. Weber, N. H. Menzler, and B. Nestler

Cite This: https://doi.org/10.1021/acsaem.5c02218

Read Online

ACCESS | Metrics & More | Article Recommendations

ABSTRACT: The long-term durability of solid oxide fuel cells (SOFCs) requires a comprehensive understanding of electrode degradation mechanisms. Performance degradation of nickel−gadolinium-doped ceria (Ni-GDC) electrodes, however, is not yet thoroughly understood, limiting their effective design and advancement. Multiphase-field (MPF) simulation studies provide an effective method to understand the underlying microstructural changes and the resulting electrochemical property alterations in SOFCs over time. In this study, we present quantitative simulations of nickel and GDC coarsening in SOFC anodes employing an MPF model utilizing focused ion beam-scanning electron microscopy-reconstructed experimental 3D microstructures and reliable thermophysical parameters. The model is initialized with experimentally reconstructed pristine and preaged Ni-GDC microstructures and validated against aged experimental microstructures after 240 and 1100 operating hours. The model incorporates both surface and interface diffusivity to capture morphological evolutions. Key microstructural properties, mean particle size, three-phase boundary line density, tortuosity, and specific surface areas are evaluated to assess degradation. Furthermore, the influence of surface and interfacial energies on long-term degradation is investigated by considering distinct thermodynamic equilibrium contact angle scenarios at the triple junction and investigating layer formation around particles in Ni-GDC systems.

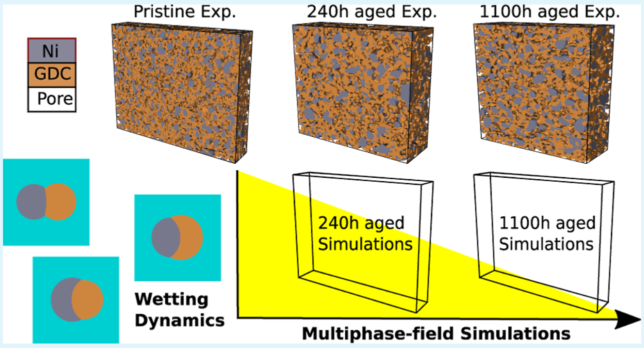

KEYWORDS: *solid-oxide fuel cells, phase-field modeling, Ni−GDC anode, coarsening, wetting, surface and interface diffusion, validation, FIB-SEM 3D microstructures*

1. INTRODUCTION

Solid oxide fuel cells (SOFCs) are attracting a growing amount of attention considering their high efficiency at elevated operating temperatures (600 °C−900 °C).[1,2] Fuel cells play a crucial role in sustainable power generation by directly converting chemical energy into electricity.[3,4] Nevertheless, large-scale commercialization of these fuel cells is limited by the high costs and long-term stability.[5] By lowering the operating temperature (<650 °C), more cost-effective materials and improved durability can be attained. Conventional nickel/yttria-stabilized zirconia (Ni-YSZ) cermet anodes, manufactured by ceramic processing, experience performance limitations at lower temperatures owing to the low ionic conductivity of yttria-stabilized zirconia (YSZ), resulting in increased ohmic resistance.[6,7] Therefore, alternative materials and electrode designs are required to maintain efficiency and stability at intermediate temperature conditions.[6] Ni/Ceria-based anodes offer a promising solution, primarily due to the superior ionic conductivity of gadolinia-doped ceria even at lower temperatures of 500 °C.[7,8] In Ni-YSZ SOFC anodes, electrochemical reactions take place at the triple-phase boundary (TPB), which is defined as the line or region where the electron, ion, and gas phase intersect. TPBs are the primary electrochemical reaction sites where fuel cell reactions occur, and a higher TPB density improves fuel cell performance. In contrast, Ni-GDC anodes also utilize the double-phase boundary (DPB), i.e., the GDC/gas interface. Since GDC is a mixed ionic-electronic conductor, the DPB interface also supports electrochemical reactions, extending the region of electrochemical reactions beyond the TPBs and enabling over a larger surface area compared to the Ni-YSZ anode.[9−11] The distribution and stability of these active sites

Received: July 18, 2025
Revised: September 14, 2025
Accepted: September 15, 2025

over long-term operating hours are critical for maintaining the durability and performance of the cells.

The degradation of Ni-based cermet anodes arises from several phenomena, including poisoning by fuel impurities,[12] coking,[13] redox cycling,[14−16] and microstructural evolution.[17] In terms of microstructural degradation, the coarsening of nickel particles is found to be the primary degradation mechanism in the microstructure of SOFC anodes.[18,19] Furthermore, polarization effects also influence Ni morphology, as demonstrated by Jiao and Shikazono,[20] observing Ni spreading along the YSZ surface near active TPBs in patterned Ni film anodes. Several studies investigated the morphological changes observed in commonly used anodes, with aging primarily caused by Ni coarsening, agglomeration, and depletion.[21−23] In contrast to the relatively stable zirconia matrix in Ni-YSZ systems, Ni-GDC anodes exhibit notable GDC phase evolution.[21,24] Several experimental studies reported findings under electrochemically operated conditions,[21,25,26] whereas some were performed under purely thermal/open-circuit voltage (OCV) conditions.[24,27] Under polarized conditions, Zekri et al.[21] reported a significant GDC agglomeration after 20,000 h, which reduced the Ni−Ni and Ni−GDC contacts, decreasing the TPB density and increasing the electronic resistance. Their work also reported the formation of a GDC coating on Ni surfaces after about 15,000 h, which suppresses Ni coarsening but hinders mass transfer, further reducing TPB density and Ni percolation. Holzer et al.[24] reported similar Ni surface coverage after only 2286 h under humidified OCV conditions. Recently, Liu et al.,[27] also under humidified, OCV conditions, reported Ni coarsening associated with minor GDC growth but found no evidence of nano-GDC particles or nanoscale changes in the GDC phase. In addition, operando studies highlighted Ni migration, spreading, and splitting at active TPB sites in both Ni-YSZ and Ni-GDC systems under polarization.[25,26] This work employs reconstructed electrode microstructures from a cell aged purely under thermal humidified open-circuit conditions for model validation. Understanding the relationship between these microstructural evolutions and the degradation of electrochemical performance is essential for improving the SOFC durability and optimizing the anode design.

The coarsening of Ni in solid oxide cell (SOC) electrodes by phase-field modeling (PFM) is extensively studied.[28−39] Most models assume nickel self-diffusion, either in the volume or at the surface, driven by curvature effects. The early work by Chen et al.[28] used focused ion beam-scanning electron microscopy (FIB-SEM)-reconstructed 3D microstructures with limited size and investigated the influence of wettability on microstructural evolution, a topic that was further explored in the work by Li et al.,[29] Davis et al.,[30] Jiao and Shikazono,[32] Lei et al.,[35] and Sun et al.[38] Ni coarsening in SOC electrodes is known to proceed significantly more quickly in a humid atmosphere, though the underlying mechanisms are not yet fully understood. Lei et al.[33,35,39] investigated Ni migration driven by $Ni(OH)_2$ diffusion, and changes in Ni-YSZ wettability were investigated using a multiphysics model. They reported that the accelerated coarsening under humid conditions cannot be explained by the diffusion of $Ni(OH)_2$ alone. Instead, the electrochemical formation of $Ni(OH)_x$ at high overpotentials may enhance Ni transport in the fuel cell mode. It is noteworthy to mention that these phase-field studies were primarily focused on Ni-YSZ systems where Ni evolves while YSZ remains structurally stable. In contrast, limited phase-field studies are available in the literature for Ni-GDC systems, where both Ni and GDC evolve, resulting in complex microstructural changes compared to Ni-YSZ. Recently, Sun et al.[40] developed an integrated mesoscale model to predict the morphological and performance degradation of Ni-GDC over long-term operation. In their study, the phase-field model was utilized to simulate compositional changes, considering the interactions between Ni-GDC and wettability. In this work, synthetic microstructures were used, and the model results were validated against experimental data from the literature of Holzer et al.[24] Previous work, while informative, relied on indirect validation involving only three microstructural properties (mean particle diameters of nickel, GDC, and TPBs) from literature data. In contrast, the validation strategy in this work incorporates both pristine and experimentally aged FIB-SEM 3D microstructures, allowing direct validation of all key descriptors (particle sizes, TPB densities, tortuosities, and specific surface areas—for a more comprehensive and quantitative assessment of model predictability). Furthermore, the current work also provides detailed insights into the sensitivity of surface and interfacial energies, their role in morphological evolution, and the resulting impact on anode performance with large-scale phase-field simulations.

Phase-field models of SOC coarsening were implemented with different mass transport mechanisms, ranging from predominant surface diffusion at Ni/pore interfaces[28,31] to the combination of interfacial diffusion across multiple phase boundaries.[30] In the early models, the multiphase Cahn−Hilliard model[41] and the combination of Allen−Cahn and Cahn−Hilliard formulations[42,43] were mostly employed. Lei et al.[44] advanced the Chen−Fan model[45] toward tunable interfacial energies and consistent interfacial thicknesses, allowing for a more accurate representation of wetting conditions in evolving microstructures. The phase-field model utilized in this work, developed by Choudhury and Nestler[46] and extended by Hoffrogge et al.,[47] provides several key advantages. It allows the interfacial energies to be controlled independently for each binary interface while maintaining uniform and finite interface thicknesses. Furthermore, the model enables an accurate representation of interfacial diffusion, facilitating the direct incorporation of experimentally measured surface diffusivities and wetting angles into the simulations. Hoffrogge et al.[36] employed this model to investigate the coarsening in FIB-SEM-reconstructed Ni-YSZ anodes and the role of Ni wettability on YSZ. Simulated results were used as inputs to an established transmission line model to predict performance degradation. Here, the YSZ phase was treated as stationary, and Ni transport along the Ni/YSZ interfaces was negligible due to a lack of experimental data. In their work, although the results presented were not validated directly against aged FIB-SEM 3D reconstructions of Ni-YSZ microstructures, the quantitative evolution of microstructural properties was reported and stated to be consistent with experimental observations and the available literature. None of the previous phase-field studies for Ni-GDC systems integrated realistic experimental microstructures and quantitative validation against the experimentally aged data.

In this work, we aim to perform quantitative 3D phase-field simulations of Ni and GDC coarsening in Ni-GDC SOFC anodes, employing an MPF model initialized with experimentally reconstructed 3D pristine microstructures and validated against experimentally aged microstructures (240 and 1100 h). To accurately predict degradation with the PFM, reliable interface and diffusion parameters are required, which were derived in our previous work[48] through a Bayesian active learning (AL) framework, as the literature data for Ni-GDC is scarce. Investigated simulation studies include both surface diffusion and interfacial diffusion along the Ni/GDC interface. By employing both pristine and preaged microstructures as input, the predictive capability of the model under different initial conditions is evaluated. Validation is performed by comparing the evolution of mean particle sizes, TPB densities, tortuosities, and specific surface areas with experimental data. Considering the operation-dependent wetting behavior of Ni-GDC observed by Holzer et al.[24] and Zekri et al.,[21] we also investigate the sensitivity of the microstructural evolution to surface and interfacial energy variations, considering three thermodynamic equilibrium states.

2. METHODS

In this section, we present a detailed methodology for modeling and simulating the coarsening behavior of Ni-GDC anodes in SOFCs. The discussion begins with an overview of the preparation of the Ni-GDC anode samples and their operating conditions. This is followed by a description of acquiring 3D microstructural data using FIB-SEM. Afterward, the formulations and assumptions underlying the modeling of coarsening phenomena are explained. Thereafter, key physical parameters specific to Ni-GDC anodes are discussed along with model parametrization and microstructural quantification.

2.1. Cell Fabrication. Symmetrical cells consisting of an 8YSZ electrolyte sandwiched between GDC interlayers were produced at the Forschungszentrum Jülich GmbH (FZJ). The GDC powder ($Gd_{0.1}Ce_{0.9}O_{1.95}$) transformed into a paste. Therefore, α-terpineol was used as a dispersion medium and ethylcellulose as a transport medium. The NiO/GDC functional layer was produced in the same way, using GDC powder ($Gd_{0.1}Ce_{0.9}O_{1.95}$) and NiO powder in a 50:50 w % ratio. An additional contact layer of NiO was added on top using the screen-printing method and dried at 80 °C overnight.

2.2. Operating Conditions for Tested Cells. The cells described in Section 2.1 were heated to 800 °C under a nitrogen atmosphere at a heating rate of 3 K min^{-1} and then gradually reduced using hydrogen/nitrogen gas mixtures at the Karlsruhe Institute of Technology (KIT). Once the gas composition was adjusted to a hydrogen flow of 0.5 L min^{-1} and oxygen flow of 0.125 L min^{-1}, creating a hydrogen/steam mixture with a 1:1 ratio in the upstream burner,[49] the cells were characterized via electrochemical impedance spectroscopy at temperatures of 800, 650, and 600 °C. Following this initial characterization, the furnace temperature was increased to achieve a cell temperature of 900 °C. The evolution of cell performance was monitored through continuous impedance measurements, which were conducted under open-circuit voltage (OCV) conditions to ensure the electrochemical symmetry of both electrodes. This study employed the active-driven gas layer concept, as detailed in ref 27. Further descriptions of the sample holder and other components of the testbench are available in refs 27 and 49, respectively. Three cells from the same production batch were evaluated. Cell A (pristine) underwent reduction but was not subjected to aging. Cell B (240 h aged) was operated at 900 °C for 240 h, while Cell C (1100 h aged) was operated for 1100 h at the same elevated temperature. Following the operation, the cells were cooled to room temperature in a reducing atmosphere ($H_2/N_2 = 0.05:0.95$).

2.3. Reconstruction of Pristine and Aged 3D Microstructures. The 3D microstructure data used in this work were reconstructed from Ni-GDC anode samples fabricated at FZJ and artificially aged at KIT, as reported by Liu et al.[27] The experimental cells employed in this work differ from samples reported in ref 27, though cells originate from the same batch and were tested under identical conditions. Sample preparation involved infiltration of pores with electrically conductive epoxy resin, metallographic sectioning, and micropreparation with a focused ion beam. A Plasma-FIB system was then employed to acquire alternating SEM images and sequential slices. The resulting grayscale image stack was denoised using a Split-Bregman optimization method and segmented via a watershed algorithm. For effective watershed seeding, a tailored procedure was implemented to extract threshold values from the grayscale histogram and eliminate markers near high-gradient regions and ridge-like features, using a Meijering filter.

2.4. Multiphase-Field Model for Coarsening of Nickel and GDC. This study employs a simplified modeling approach that captures the essential physical mechanisms of coarsening in Ni-GDC anodes while maintaining the computational efficiency. The model is based on the following assumptions:

- conservation of mass and volume: the mass and volume (phase fractions) of Ni and GDC are assumed to remain constant during the coarsening process. This assumption is justified by the negligible evaporation of Ni at typical operating temperatures of solid oxide cells (500 to 1000 °C).[34,50]
- Isotropic interfacial properties: the interfacial energy and diffusion coefficients are treated as isotropic and constant. This simplification allows for neglecting the effects of crystal orientation on the interfacial energies and diffusion coefficients of Ni and GDC.
- Mass transport mechanisms: surface and interfacial diffusion are considered as the primary mass transport mechanisms, and contributions from bulk diffusion are negligible for both Ni and GDC. This assumption is based on the higher diffusion rates typically observed along surfaces and interfaces compared to bulk diffusion in materials at the temperatures considered here.[51]
- Coarsening of both Ni and GDC as a degradation mechanism: as discussed in the Section 1, Ni-GDC anodes exhibit significant GDC phase evolution in addition to Ni coarsening. Previous studies reported pronounced GDC agglomeration after 20,000 h and GDC coating formation on Ni surfaces at around 15,000 h.[21] Liu et al.[27] observed Ni coarsening and little GDC growth, with no evidence of nanoscale GDC features. In this study, the coarsening of Ni and GDC is assumed to be the main degradation mechanism, and the GDC coating-like formation is investigated by surface and interfacial energy sensitivity analysis in Ni-GDC systems.

These assumptions enable a focus on the main physical processes driving microstructural evolution in Ni-GDC anodes, while maintaining a tractable model. Although these assumptions may introduce some limitations, they provide a reasonable balance between model accuracy and computational feasibility for large-scale simulations of the coarsening behavior in SOFC anodes with larger domain sizes. The current work therefore focuses only on investigating the effects of the coarsening of Ni and GDC particles on the microstructural evolution of the anode and, thereby, on the SOFC performance in long-term operation.

A multiphase-field model based on the grand-potential functional developed by Choudhury and Nestler[46] and subsequently extended to incorporate surface self-diffusion effects[47] is employed in this work. This model enables simulation of the coarsening dynamics of Ni and GDC phases. The formulation is essentially centered on the grand-potential functional, denoted as Ω (in J), representing the energetic state of a system of volume V. This functional is expressed in terms of the order parameters $\boldsymbol{\phi} = \{\phi_\alpha, \phi_\beta, ..., \phi_N\}$ (dimensionless) for N distinct phases and the volumetric chemical potentials $\boldsymbol{\mu} = \{\mu_1, \mu_2, ..., \mu_{K-1}\}$ (in J m^{-3}) for K chemical components, as follows:

$$\Omega(\boldsymbol{\phi}, \nabla\boldsymbol{\phi}, \boldsymbol{\mu}) = \int_V \frac{1}{\epsilon} w(\boldsymbol{\phi}) + \epsilon a(\nabla\boldsymbol{\phi}) + \psi(\boldsymbol{\phi}, \boldsymbol{\mu})\, \mathrm{d}V \tag{1}$$

Here, $w(\boldsymbol{\phi})$ (in J m^{-2}), $a(\nabla\boldsymbol{\phi})$ (in J m^{-4}), and $\psi(\boldsymbol{\phi}, \boldsymbol{\mu})$ represent the potential, gradient, and bulk energy contributions, respectively. The parameter ϵ (in m) determines the diffuse interface width, defined as $\delta = \epsilon\pi^2/4$. To account for the interfacial energy and to stabilize the interface profile with a finite thickness, the combined potential and gradient terms as given in ref 52 are incorporated. The potential term ensures that the order parameters remain within a thin and defined diffuse interface thickness range and captures the interfacial energy contribution. In this study, we adopted an obstacle potential with the following formulation

$$w(\boldsymbol{\phi}) = \begin{cases} \dfrac{16}{\pi^2} \displaystyle\sum_{\substack{\alpha,\beta=1 \\ \alpha<\beta}}^{N,N} \gamma_{\alpha\beta}\phi_\alpha\phi_\beta, & \boldsymbol{\phi} \in \mathcal{G} \\ \infty, & \boldsymbol{\phi} \notin \mathcal{G} \end{cases} \tag{2}$$

where $\gamma_{\alpha\beta}$ (in J m^{-2}) represents the interfacial energy between phases α and β. The Gibbs simplex $\mathcal{G}$ is defined as

$$\mathcal{G} = \left\{ \sum_{\alpha=1}^{N} \phi_\alpha = 1 \colon \{\phi_\alpha \geq 0, \forall\, \alpha \in \{1, ..., N\}\} \right\} \tag{3}$$

This ensures that the order parameters ϕ_α remain non-negative and their sum equals unity. In addition, the gradient term incorporates interfacial energy into the system and stabilizes the profile of diffuse interfaces with a finite thickness. Following the formulation in ref 53, the gradient term is given as

$$a(\nabla\boldsymbol{\phi}) = -\sum_{\substack{\alpha,\beta=1 \\ \alpha<\beta}}^{N,N} \gamma_{\alpha\beta}\nabla\phi_\alpha \cdot \nabla\phi_\beta \tag{4}$$

where $\nabla\phi_\alpha$ and $\nabla\phi_\beta$ are the gradients of the order parameters. Hoffrogge et al.[54] demonstrated that the combination of eqs 4 and 2 correctly reflects Young's law up to negligible deviations. The bulk grand-potential density is expressed as an interpolation of the grand-potential densities of individual bulk phases. It is given by

$$\psi(\boldsymbol{\phi}, \boldsymbol{\mu}) = \sum_{\alpha=1}^{N} \psi^\alpha(\boldsymbol{\mu}) h_\alpha(\boldsymbol{\phi}) \tag{5}$$

where the grand-potential density for phase α is described as

$$\psi^\alpha(\boldsymbol{\mu}) = f^\alpha(\boldsymbol{c}^\alpha(\boldsymbol{\mu})) - \sum_{i=1}^{K-1} \mu_i c_i^\alpha(\boldsymbol{\mu}), \quad \forall\, \alpha \in \{1, ..., N\} \tag{6}$$

The bulk free energy f^α corresponds to phase α, which depends on the phase-specific compositions $c^\alpha = \{c_1^\alpha, c_2^\alpha, ..., c_{K-1}^\alpha\}$. In this study, the interpolation function h_α is chosen to be $h_\alpha(\boldsymbol{\phi}) = \phi_\alpha$, ensuring the constraint $\sum_{\alpha=1}^{N} h_\alpha(\boldsymbol{\phi}) = 1$ is satisfied. A local quasi-equilibrium assumption is applied, ensuring that, at every spatial location, the condition

$$\mu_i = \frac{\partial f^\alpha(c^\alpha)}{\partial c_i^\alpha} = \frac{\partial f^\beta(c^\beta)}{\partial c_i^\beta} = \cdots = \frac{\partial f^N(c^N)}{\partial c_i^N} \tag{7}$$

is met for all $i \in \{1, ..., K-1\}$.

According to ref 53, the evolution equation of each phase-field ϕ_α is specified as

$$\epsilon\frac{\partial\phi_\alpha(x, t)}{\partial t} = \frac{1}{\tilde{N}} \sum_{\substack{\beta=1 \\ \beta\neq\alpha}}^{N} m_{\alpha\beta}\left(\frac{\delta\Omega}{\delta\phi_\beta} - \frac{\delta\Omega}{\delta\phi_\alpha}\right) \tag{8}$$

In this context, $\tilde{N}$ denotes the local number of phases, while $m_{\alpha\beta}$ (with units of m^4/(J·s)) represents the mobility of the interface between α and β phases. The terms $\delta\Omega/\delta\phi_\alpha$ and $\delta\Omega/\delta\phi_\beta$ refer to the variational derivatives with respect to ϕ_α and ϕ_β. Ni and GDC are modeled as pure solids with nearly fixed compositions. Their free energies are introduced in the form $f^\alpha(\boldsymbol{c}^\alpha(\boldsymbol{\mu})) = \sum_{i=1}^{K-1} f_i^\alpha(c_i^\alpha)$, where each contribution is assumed to follow the simple parabolic form $f_i^\alpha(c_i^\alpha) = A_i[c_i^\alpha(\mu_i) - c_{i,\mathrm{eq}}^\alpha]^2$ for $i \in \{\mathrm{Ni, GDC}\}$. The prefactor A_i characterizes the strength of the immiscibility and is chosen to be sufficiently large to ensure volume conservation within each phase. $c_{i,\mathrm{eq}}^\alpha$ denotes the equilibrium concentration of species i in phase α.

The porous Ni-GDC system is described using three distinct order parameters $\boldsymbol{\phi} = \{\phi_{Ni}, \phi_{GDC}, \phi_{Pore}\}$, representing the metallic nickel phase, the GDC structure, and the voids. For the transport of each substance, a set of two dimensionless composition variables, $\boldsymbol{c} = \{c_{\mathrm{Ni}}, c_{\mathrm{GDC}}\}$, representing the mole fractions of nickel and GDC, are employed. With $K = 3$, the composition of the porous phase is expressed as $c_{\mathrm{Pore}} = 1 - c_{\mathrm{Ni}} - c_{\mathrm{GDC}}$. For a clear distinction between the phase symbols and the component notation, italicized symbols are used to represent the phases throughout the text. The dimensionless composition fields, $c_i = \sum_{\alpha=1}^{N} h_\alpha c_i^a$ (mole fractions), are conserved quantities within the system. Conservation laws govern their evolution, ensuring mass balance consistency across the phases. The equations account for the dynamic redistribution of the composition fields during the coarsening process and are expressed as follows

$$\frac{\partial c_i(\boldsymbol{x}, t)}{\partial t} = -\nabla\cdot\boldsymbol{j}_i \tag{9}$$

Here, $\boldsymbol{j}_i$ represents the flux of species i, measured in units of m s^{-1}. The evolution of the chemical potential can be expressed using Einstein's notation as

$$\frac{\partial \mu_i(\boldsymbol{x}, t)}{\partial t} = \left[\sum_{\alpha=1}^{N} h_\alpha(\boldsymbol{\phi}) \frac{\partial c_j^\alpha(\boldsymbol{\mu})}{\partial \mu_i}\right]^{-1} \left[\frac{\partial c_j(\boldsymbol{x}, t)}{\partial t} - \sum_{\alpha=1}^{N} c_j^\alpha(\boldsymbol{\mu}) \frac{\partial h_\alpha(\boldsymbol{\phi}(\boldsymbol{x}, t))}{\partial t}\right] \quad (10)$$

In SOFC anodes, surface diffusion is assumed as the dominant mechanism for mass transfer within the typical operating temperature range. In contrast to Ni-YSZ anodes, Ni-GDC anodes demonstrate coarsening behavior for both Ni and GDC over time.[21] This model extends the analysis by incorporating both surface diffusion and diffusion along the interface between nickel and GDC. The inclusion of additional diffusion pathways provides a more comprehensive representation of the mass transfer processes within Ni-GDC anodes. Consequently, the flux density of nickel is derived as follows:

$$\boldsymbol{j}_{\mathrm{Ni}} = -\frac{32}{\pi^2 \epsilon} \nabla \mu_{\mathrm{Ni}} (M_{\mathrm{Ni}}^{NiPore} \phi_{Ni} \phi_{Pore} + M_{\mathrm{Ni}}^{NiGDC} \phi_{Ni} \phi_{GDC}) \quad (11)$$

The diffusion of nickel along the tangential direction of the free nickel surface and the diffusion along the Ni/GDC interface are determined by the mobilities M_{Ni}^{NiPore} and M_{Ni}^{NiGDC} with the units $\mathrm{m}^6/(\mathrm{J \cdot s})$. These mobilities are directly related to the surface self-diffusivity D_{Ni}^{NiPore} and the interfacial self-diffusivity D_{Ni}^{NiGDC} by an Einstein-like relationship as described in (cf. [47, eq 99 ff.]), which is expressed as follows:

$$M_{\mathrm{Ni}}^{NiPore} = \frac{D_{\mathrm{Ni}}^{NiPore} \delta_{\mathrm{s}} V_{\mathrm{m}} (\Delta c_{\mathrm{Ni,eq}}^{Ni-Pore})^2}{RT} \quad (12)$$

$$M_{\mathrm{Ni}}^{NiGDC} = \frac{D_{\mathrm{Ni}}^{NiGDC} \delta_{\mathrm{I}} V_{\mathrm{m}} (\Delta c_{\mathrm{Ni,eq}}^{Ni-GDC})^2}{RT} \quad (13)$$

The atomistic thicknesses of the surface (δ_{s}) and the interface (δ_{I}) are approximately 0.1 nm. Nickel's molar volume (V_{m}) is included in the formulation, along with the ideal gas constant (R) and temperature (T). To simplify the model and avoid arbitrary assumptions about interface thicknesses, the term excess interface diffusivity is defined. These are expressed as $D_{\mathrm{Ni,ex}}^{NiPore} \equiv D_{\mathrm{Ni}}^{NiPore} \delta_{\mathrm{s}}$ and $D_{\mathrm{Ni,ex}}^{NiGDC} \equiv D_{\mathrm{Ni}}^{NiGDC} \delta_{\mathrm{I}}$, respectively, both measured in m^3/s. The model-specific composition differences $\Delta c_{\mathrm{Ni,eq}}^{Ni-Pore}$ and $\Delta c_{\mathrm{Ni,eq}}^{Ni-GDC}$ are specified as $\Delta c_{\mathrm{Ni,eq}}^{Ni-Pore} \equiv c_{\mathrm{Ni,eq}}^{Ni} - c_{\mathrm{Ni,eq}}^{Pore} = 0.8$ and $\Delta c_{\mathrm{Ni,eq}}^{Ni-GDC} \equiv c_{\mathrm{Ni,eq}}^{Ni} - c_{\mathrm{Ni,eq}}^{GDC} = 0.8$, respectively. Similarly, the flux density of GDC and the corresponding mobilities are expressed as

$$\boldsymbol{j}_{\mathrm{GDC}} = -\frac{32}{\pi^2 \epsilon} \nabla \mu_{\mathrm{GDC}} (M_{\mathrm{GDC}}^{GDCPore} \phi_{GDC} \phi_{Pore} + M_{\mathrm{GDC}}^{NiGDC} \phi_{GDC} \phi_{Ni}) \quad (14)$$

$$M_{\mathrm{GDC}}^{GDCPore} = \frac{D_{\mathrm{GDC}}^{GDCPore} \delta_{\mathrm{s}} V_{\mathrm{m}} (\Delta c_{\mathrm{GDC,eq}}^{GDC-Pore})^2}{RT} \quad (15)$$

$$M_{\mathrm{GDC}}^{NiGDC} = \frac{D_{\mathrm{GDC}}^{NiGDC} \delta_{\mathrm{I}} V_{\mathrm{m}} (\Delta c_{\mathrm{GDC,eq}}^{Ni-GDC})^2}{RT} \quad (16)$$

At the domain boundaries, zero-flux boundary conditions are enforced, treating them as isolating (i.e., $\boldsymbol{j}_i \cdot \boldsymbol{n} = 0 \; \forall \; i, x \in \mathrm{d}V$), where $\boldsymbol{n}$ denotes the normal to the domain boundary, which means there is no net flux across the boundary. In addition, a perpendicular contact condition for the order parameter is assumed ($\nabla \phi_\alpha \cdot \boldsymbol{n} = 0$), which ensures that the gradient of the order parameter is normal to the boundary. In this manuscript, a SIMD-vectorized solver is used, the implementation of which is described in detail in [55, Section 4.2]. The interested reader is referred to refs 47 and 36 for model validation. To establish a stable and physically consistent initial condition for our phase-field simulations, we employed a preconditioning algorithm that generates a diffuse interface profile. This step aims to generate a sinusoidal and sufficiently diffuse interface at the boundary between the phases. Following the approach described in ref 56, this is achieved by omitting the curvature term in the evolution equation and in the absence of any chemical driving force. Preconditioning is performed over a sufficient number of iterations to ensure a stable profile characterized by a constant interface width.

2.5. Model Parametrization and Bayesian AL for Physical Parameters. Accurately simulating the aging process in Ni−GDC anodes and reliably predicting their long-term behavior under operating conditions require accurate parametrization of the phase-field model. However, the scarcity and inconsistency of the literature data render this task considerably more challenging, especially for critical parameters such as surface diffusivities and interfacial energies for the Ni-GDC system. Although data for similar systems such as Ni-YSZ can be obtained from the literature, these details are not available for Ni-GDC, which presents a significant challenge. To address these limitations, we implemented an AL framework with integrated Bayesian optimization in our previous work.[48] This approach was specifically designed to efficiently navigate the high-dimensional parameter space and enable the identification of optimal model parameters for simulating the aging behavior of Ni-GDC anodes. With the help of this framework, we identified a promising set of parameter values that not only optimize the model but also match the existing literature's data. From the parameter optimization of the AL-Bayesian framework, we obtained interfacial energy values of γ_{NiGDC}, $\gamma_{\mathrm{GDCPore}}$, and γ_{NiPore} as 2.43, 1.43, and 2.10 $\mathrm{J/m^2}$, respectively. These values are consistent with the literature-reported surface energies. For nickel, surface energies are reported in the range of 1.6−2.5 $\mathrm{J/m^2}$.[57−60] Similarly, the surface energies of GDC for the {100}, {110}, and {111} orientations are 1.46, 0.90, and 0.74 $\mathrm{J/m^2}$, respectively, as reported in ref 61. Experimental studies employing the multiphase equilibration technique estimated the surface energy of $\mathrm{CeO_2}$ in an argon atmosphere at 900 °C to be approximately 1.80 $\mathrm{J/m^2}$ through extrapolation.[62] Additionally, the optimized excess surface and interface diffusivities for the Ni-GDC system were determined as follows: $D_{\mathrm{Ni,ex}}^{NiPore}$, $D_{\mathrm{Ni,ex}}^{NiGDC}$, $D_{\mathrm{GDC,ex}}^{GDCPore}$, and $D_{\mathrm{GDC,ex}}^{NiGDC}$, with values of 4.0×10^{-22}, 4.0×10^{-27}, 4.96×10^{-27}, and 1.14×10^{-33} $\mathrm{m^3\,s^{-1}}$, respectively, from the AL Bayesian framework. These values correspond to operating conditions for Ni-GDC anodes at a temperature of 900 °C with a gas composition of 50% $\mathrm{H_2}$/50% $\mathrm{H_2O}$ in the SOFC mode.

For simplification of the analysis, the parameters of the phase-field model are represented in a model-specific system of units where u_l, u_E, and u_t denote the characteristic units of length, energy, and time, respectively. The length unit u_l is determined by the resolution of the original microstructure (Δx). The units of energy and time are linked by the surface energy of the nickel, γ_{NiPore}, the surface diffusivity of the nickel, D_{Ni}^{NiPore}, and the operating temperature, T (refer to eq 12). A detailed parametrization of the model can be found in Table 1.

Table 1. Phase-Field Model Parameters Employed in the Coarsening Simulations of the Ni-GDC Anode[a]

parameter (symbol)	value (model units)	value (physical units)	source
Ni−surf. chem. mobility (M_{Ni}^{NiPore})	0.1 $u_l^6/(u_E \cdot u_t)$	1.73×10^{-31} $m^6/(J \cdot s)$	ref 48
Ni−Ni/GDC interf. chem. mobility (M_{Ni}^{NiGDC})	1.0×10^{-6} $u_l^6/(u_E \cdot u_t)$	1.73×10^{-36} $m^6/(J \cdot s)$	ref 48
GDC−surf. chem. mobility ($M_{\mathrm{GDC}}^{GDCPore}$)	4.37×10^{-6} $u_l^6/(u_E \cdot u_t)$	7.55×10^{-36} $m^6/(J \cdot s)$	ref 48
GDC−Ni/GDC interf. chem. mobility (M_{GDC}^{NiGDC})	1.0×10^{-12} $u_l^6/(u_E \cdot u_t)$	1.73×10^{-42} $m^6/(J \cdot s)$	ref 48
interfacial energy Ni/pore (γ_{NiPore})	1.0 u_E/u_l^2	2.1 J/m^2	ref 48
interfacial energy Ni/GDC (γ_{NiGDC})	1.16...0.47 u_E/u_l^2	2.43...0.98 J/m^2	ref 48
interfacial energy GDC/pore ($\gamma_{GDCPore}$)	0.68...1.87 u_E/u_l^2	1.43...3.92 J/m^2	ref 48
interface mobility Ni/pore (m_{NiPore})	0.1 $u_l^4/(u_E \cdot u_t)$	6.92×10^{-17} $m^4/(J \cdot s)$	refs 36, 47, 48
interface mobility Ni/GDC (m_{NiGDC})	0.1 $u_l^4/(u_E \cdot u_t)$	6.92×10^{-17} $m^4/(J \cdot s)$	refs 36, 47, 48
interface mobility GDC/pore (m_{GDCPore})	0.1 $u_l^4/(u_E \cdot u_t)$	6.92×10^{-17} $m^4/(J \cdot s)$	refs 36, 47, 48
interface width parameter (ϵ)	2.0 u_l	100 nm	refs 36, 47, 48
voxel-size ($\Delta x = \Delta y = \Delta z$)	1.0 u_l	50 nm	experimental data
thermodynamic prefactor nickel (A_{Ni})	5 u_E/u_l^3	2.1×10^8 J/m^3	refs 36, 47, 48
thermodynamic prefactor GDC (A_{GDC})	50 u_E/u_l^3	2.1×10^9 J/m^3	refs 36, 47, 48
equil.-comp. Ni−Ni ($c_{\mathrm{Ni,eq}}^{Ni}$)	0.9	90 mol %	refs 36, 47, 48
equil.-comp. Ni−GDC ($c_{\mathrm{Ni,eq}}^{GDC}$)	0.1	10 mol %	refs 36, 47, 48
equil.-comp. Ni−pore ($c_{\mathrm{Ni,eq}}^{Pore}$)	0.1	10 mol %	refs 36, 47, 48
equil.-comp. GDC−Ni ($c_{\mathrm{GDC,eq}}^{Ni}$)	0.1	10 mol %	refs 36, 47, 48
equil.-comp. GDC−GDC ($c_{\mathrm{GDC,eq}}^{GDC}$)	0.9	90 mol %	refs 36, 47, 48
equil.-comp. GDC−pore ($c_{\mathrm{GDC,eq}}^{Pore}$)	0.1	10 mol %	refs 36, 47, 48

[a] These parameters are derived from the physical properties of the material system and represented in a model-specific system of units. The model units are stated as $u_l = 50$ nm, $u_E = 5.25 \times 10^{-15}$ J, and $u_t = 1.72$ s. Physical parameter values for both surface and interfacial diffusion coefficients and energies at a temperature of 900 °C with a gas composition of 50% H_2/50% H_2O were adopted from our earlier work[48] and converted into the corresponding model parameters. Other model parameters were selected following the works of refs 36, 47, 48.

The interfacial mobilities, $m_{\alpha\beta}$, are selected to remain sufficiently low to ensure that the system operates in the surface diffusion-controlled regime (cf. [47, eq 99 ff]), thus preventing these mobilities from becoming the dominant rate-limiting factors. Equilibrium compositions $c_{i,\mathrm{eq}}^{\alpha}$, which correspond to the minima of the parabolic free energy function, are assigned distinct values of 0.1 and 0.9, allowing a clear distinction between the phases, such as Ni-rich and Ni-poor regions. The prefactor A_i in the parabolic free energy formulation, which characterizes the strength of immiscibility, is chosen to ensure consistent volume conservation throughout the simulation.

For the investigation of the influence of different scenarios of contact angles, the following selection strategy is considered. Since both the Ni and GDC phases evolve over time in these systems, scenarios in which Ni transitions from dewetting to wetting and a similar transition for GDC are investigated independently. Sufficient differences in contact angles are chosen between the simulation cases to ensure that any trends observed in the results draw reliable conclusions about variations in the contact angle. While smaller contact angles such as 60° or 75° may not be achievable experimentally without particular additives or preparation, this current study provides valuable insight into whether improved wetting characteristics could contribute to mitigating anode-side degradation. It should be noted that experimental findings of Ni-GDC in the literature reported on the formation of a GDC layer around the nickel,[21,24] and the present investigation may provide additional insight into such dynamics. Nevertheless, it is important to note that exploring the practical feasibility of improving the wetting properties of nickel or GDC in Ni-GDC systems is beyond the scope of this manuscript.

Table 2. Structural Properties of Pristine, 240 h Aged, and 1100 h Aged FIB-SEM 3D-Reconstructed Experimental Microstructures of the Ni-GDC Anode

parameter	symbol	pristine exp	240 h aged exp	1100 h aged exp
Ni vol %	V_{Ni}	22.44	22.43	21.87
GDC vol %	V_{GDC}	41.38	39.84	40.81
pore vol %	V_{Pore}	36.18	37.73	37.32
total volume (μm^3)	V	6666	4800	5104
voxel size (μm)	$\Delta x = \Delta y = \Delta z$	0.05	0.05	0.05

2.6. Microstructure Quantification of the 3D Ni-GDC Anode.

The microstructural features of the 3D Ni-GDC porous anode—including median particle diameters derived from continuous particle size distributions, phase volume fractions, specific surface areas, tortuosity, and TPB lengths—were accurately characterized using established analytical techniques (Table 3). Particle coarsening analysis employs continuous particle size distributions, as described by Münch and Holzer.[63] The median particle size (d_{50}), representing the midpoint of the cumulative distribution, is a key metric in this analysis. Tortuosity (τ_α) of a phase, a dimensionless measure of transport pathway complexity, is calculated as the ratio of the ideal current to the actual current in a given phase, offering a scale-invariant representation of the transport efficiency.[64] The mean tortuosity of a phase is computed as

$$\tau_\alpha \equiv \frac{1}{3}(\tau_{\alpha,x} + \tau_{\alpha,y} + \tau_{\alpha,z}) \tag{17}$$

to capture the phases' overall transport properties. The TPB length, a crucial parameter influencing electrochemical reactions, is determined using a skeletonization algorithm.[65] Specific surface areas (A_α) for each phase are calculated by integrating the magnitude of the phase order parameter gradient:

Table 3. Microstructural Characteristic Properties of Pristine and Aged Ni-GDC Anodes: Comparative Analysis of Experimental Aging with Simulations

		240 h sim.		1100 h sim.		
parameter	pristine exp.	input: pristine	240 h exp.	input: pristine	input: preaged	1100 h exp.
Ni/pore specific area (μm^{-1})	0.37	0.31	0.33	0.29	0.29	0.31
GDC/pore specific area (μm^{-1})	1.50	1.44	1.38	1.39	1.32	1.31
Ni/GDC specific area (μm^{-1})	0.67	0.62	0.61	0.61	0.56	0.60
GDC tortuosity (−)	2.57	2.50	3.09	2.42	2.68	3.08
pore tortuosity (−)	2.57	2.55	2.36	2.59	2.37	2.38
total TPB density (μm^{-2})	1.82	1.52	1.55	1.40	1.31	1.41
nickel avg. particle dia. (μm)	0.91	0.955	1.04	0.966	1.08	1.111
GDC avg. particle dia. (μm)	0.59	0.60	0.62	0.62	0.64	0.663
pore avg. particle dia. (μm)	0.60	0.63	0.68	0.66	0.71	0.723

$$A_\alpha = \frac{1}{V} \int_V |\nabla \phi_\alpha| \, dV \tag{18}$$

with individual interface areas ($A_{\alpha/\beta}$) obtained through a system of linear equations:

$$A_{Ni} = A_{Ni/Pore} + A_{Ni/GDC} \tag{19}$$

$$A_{GDC} = A_{Ni/GDC} + A_{GDC/Pore} \tag{20}$$

$$A_{Pore} = A_{Ni/Pore} + A_{GDC/Pore} \tag{21}$$

GDC's mixed ionic and electronic conductivity highlights the significance of the GDC/Pore interface, which forms the DPB and plays a pivotal role in electrochemical reactions. All methodologies mentioned above were implemented in-house within the Parallel Algorithms for Crystal Evolution in 3D (PACE3D) Framework and validated through established test cases.[36] All of these properties are critical in determining the anode's structural and functional efficiency as they directly impact the electrochemical performance, ion and gas transport, and overall cell performance.

3. RESULTS AND DISCUSSION

This section presents the multiphase-field simulation results investigating the coarsening behavior of experimentally reconstructed FIB-SEM 3D Ni-GDC anode microstructures under specified operating conditions. We begin by validating our phase-field model by comparing the simulated aging behavior with experimental aging results, focusing on key microstructural properties. Our validation includes the utilization of two different experimental microstructures representing different aging stages as an input for phase-field simulations. Subsequently, we present a systematic phase-field simulation investigation to understand the influence of the interface energies within the Ni-GDC system with two evolving phases on the resulting microstructural properties and morphological evolutions.

3.1. Microstructural Evolution of 3D Ni-GDC Anode: Comparative Analysis of Simulation and Experimental Results. In this section, we present an analysis of microstructural evolution in Ni-GDC anodes using multiphase-field coarsening simulations and experimental results. Our approach couples 3D FIB-SEM reconstructions of experimental microstructures with PFM to predict and gain insights into the aging process of Ni-GDC anodes under high temperatures of 900 °C in a reducing atmosphere of 50% H_2/50% H_2O, without including electrochemical charge-transfer processes. Here, we employ two experimental microstructures as inputs for the phase-field simulations: a pristine Ni-GDC anode microstructure and an anode after 240 h of experimental aging. Thereafter, we perform the phase-field simulations on two distinct initial microstructures: 1100 h on the pristine microstructure (corresponding to the first validation scenario) and 860 h on the preaged microstructure (extending the predictions to two distinctive initial microstructures). With this approach, we compare the simulation results with those of experimentally aged microstructures after 240 and 1100 h. By employing pristine and preaged reference microstructures, the predictability of the model under different initial conditions is evaluated as well as the influence of local microstructural inhomogeneities on the aging behavior. This multifaceted approach enables the robust validation of our phase-field results and provides a deeper understanding of the complex microstructural evolution in Ni-GDC anodes, which is essential for predicting and optimizing the long-term performance of SOFCs.

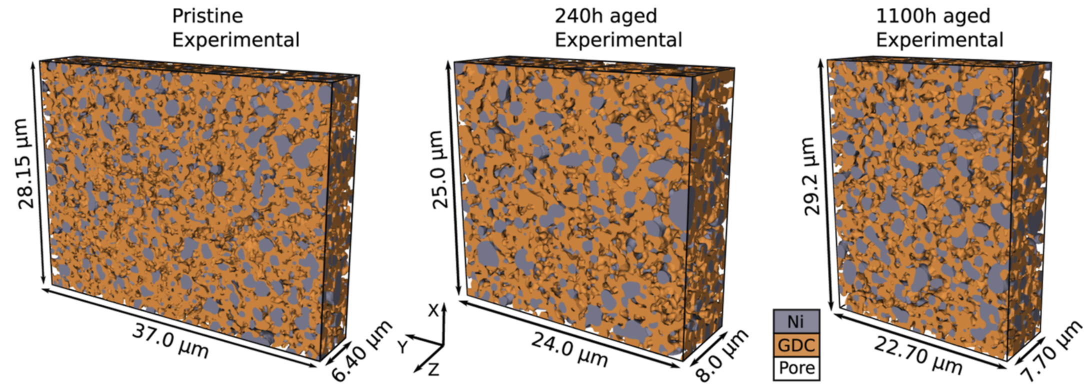

Figure 1. FIB-SEM 3D reconstructed pristine Ni-GDC anode microstructure alongside experimentally aged samples from the same batch after 240 and 1100 h.

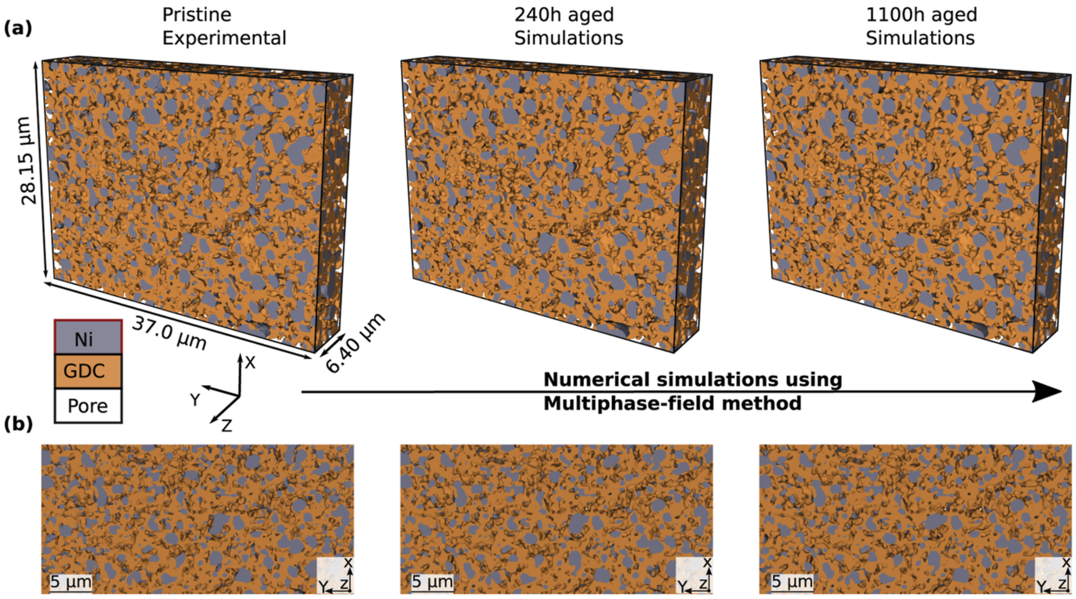

Figure 2. Phase-field simulation of the (a) 3D microstructure and (b) 2D cross sections at different aging times of 0 h, 240 h, and 1100 h using the pristine microstructure as the initial input.

Three experimental cells at different stages of aging were subjected to FIB-SEM 3D reconstructions: pristine, after 240 h of operation, and after 1100 h of operation (see Figure 1). In all three reconstructed cells, a similar composition is observed (Table 2). The differences in phase volume fractions among the pristine and aged experimental microstructures in Table 2 most probably result from slight inhomogeneities across the anode samples from the same batch. Holzer et al.[24] observed standard deviations of about 2% in the average volume fractions of all three phases in four nominally identical samples and attributed these discrepancies to sample production variations and possible preparation effects. Similar variations could thus be observed in the samples utilized for the aging experiments in this work. Liu et al.[27] also reported from experimental observations that pristine and aged cells showed fairly similar overall compositions, further indicating that these observed variations are due to minor sample-to-sample differences. These reconstructions enabled the quantification of key microstructural characteristics of the Ni-GDC anode, as shown in Table 3, and provided insight into microstructural evolution over time. The density of the TPB lines, representing electrochemically active sites, decreased from an initial value of 1.82 μm^{-2} in the pristine anode to 1.55 μm^{-2} after 240 h of operation, a reduction of 14.8%. This decrease continued during prolonged aging, with the TPB density decreasing further to 1.41 μm^{-2} after 1100 h, corresponding to an overall reduction of 22.5% compared to the initial state. Similarly, the density of the DPB area—another key parameter representing electrochemically active sites in Ni-GDC anodes—also showed a decrease in the value. The DPB density decreased from an initial value of 1.50 μm^{-1} to 1.38 μm^{-1} after 240 h, corresponding to an 8% reduction, and further decreased to 1.31 μm^{-1} after 1100 h, corresponding to an overall reduction of 12.7%.

Experimental studies showed that a higher DPB density increases the electrochemical activity in Ni-GDC anodes. Nakamura et al.[66] reported an extension of the active reaction zone beyond the TPB to the GDC/gas interface in ceria-based anodes, with an increased GDC surface area improving performance. Consistent with this, Chueh et al.,[10] utilizing well-defined ceria metal structures, demonstrated that H_2 oxidation at equilibrium occurs predominantly via electrocatalysis at the oxide/gas interface, with limited contribution from conventional TPBs. These results highlight the crucial role of DPBs (GDC/pore interfaces) in lowering the activation overpotentials for hydrogen oxidation. These observed reductions in both TPB and DPB density over aging suggest a deterioration in the overall electrochemical performance of the Ni-GDC. Although the pristine and aged microstructures were reconstructed from different domains, both microstructures correspond to the central regions of the anode, thereby minimizing edge effects and spatial heterogeneity. Statistical analysis of four nonoverlapping 1/2 subdomains of the original microstructure in our previous work[48] revealed coefficients of variation (CV) between 0 and 2% for all properties, suggesting negligible spatial variations. In addition, original microstructure volume exceeds the representative volume element threshold of 10^3 particles, above which most properties converge to stable values as reported by Joos.[67]

3.1.1. *Phase-Field Simulations of 1100 h Aging: Employing a Pristine Ni-GDC Anode as the Input.*

As described in the previous subsection, a pristine FIB-SEM-reconstructed experimental microstructure of the Ni-GDC anode was employed as the initial reference for the phase-field simulations. Aging simulations were performed for up to 1100 h, and the microstructural properties at 240 and 1100 h were compared to experimentally aged counterparts (see Table 3). A comprehensive understanding of Ni-GDC anode degradation requires analysis of several interrelated microstructural properties. To ensure accurate validation of experimental and simulated microstructural evolutions, replication of key features of the microstructure is essential. Therefore, we considered nine critical parameters: specific interface areas (Ni/Pore, GDC/Pore, and Ni/GDC), tortuosity of GDC and pore phases, TPB density, and average particle diameters of Ni, GDC, and pores.

Comparison of experimental and simulated results after 240 h of aging: the evolution of specific surface areas in the

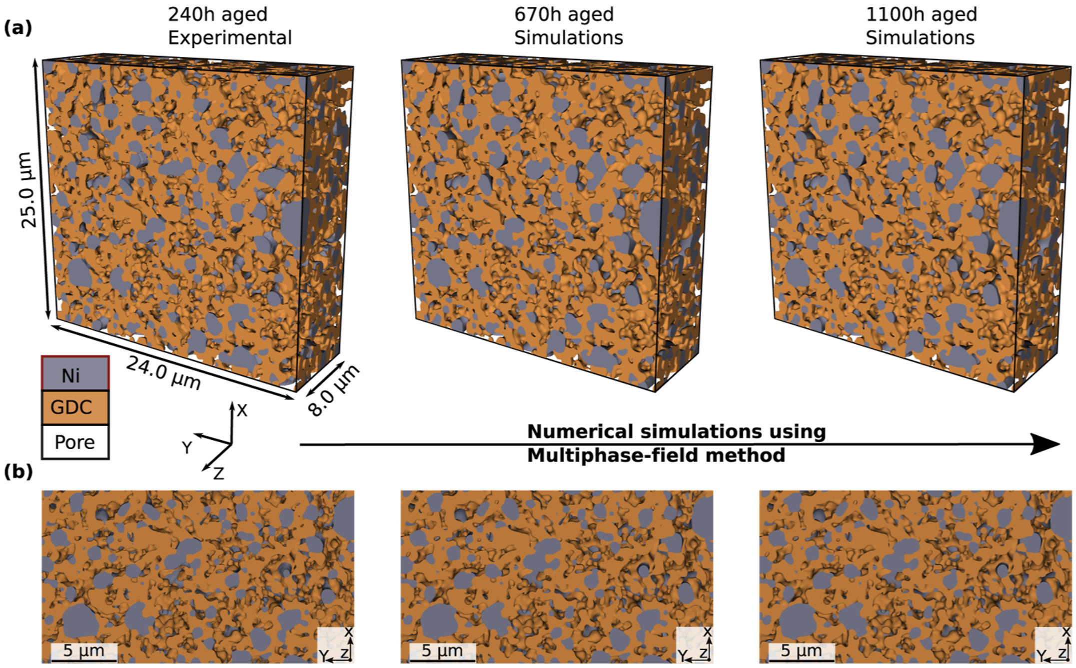

Figure 3. Phase-field simulation of the (a) 3D microstructure and (b) 2D cross sections at different aging times of 240 h, 670 h, and 1100 h using the preaged (240 h) microstructure as the initial input.

simulations aligns well with experimental data with deviations of 6% for Ni/pore and 2% for Ni/GDC interfaces. The GDC/pore interface, which presents double-phase boundaries essential for electrochemical reactions, shows a 4% deviation. The tortuosity values show larger discrepancies with deviations of 19% for GDC and 8% for pores. These differences might be due to their more localized property nature (high sensitivity against local microstructural changes) and not uniformly homogeneous transport paths across the structure. The tortuosity values for the Ni phase are not specified in Table 3 as the phase is nonpercolated. As a result of isolated and poorly connected Ni particles, the nickel phase remains sufficiently disconnected to determine a finite tortuosity value. In the literature, such instances are often stated as undefined or infinite tortuosity. The total TPB density, a key parameter for electrochemical activity, differs by about 2%, demonstrating close agreement between the phase-field simulation and experimental aging results. Experimentally, the morphological evolution of Ni and GDC during aging is observed,[21,24,27] indicated also by the increase in the mean particle diameter. The deviations in the mean particle size are 8% for Ni, 3% for GDC, and 7% for pores. Thus, except for the tortuosity of GDC, all of the microstructural characteristics predicted by the phase-field simulations remain within 8% deviation from the experimental values over the aging, demonstrating the predictive capability of our phase-field model on the microstructural evolution of Ni-GDC anodes. To further illustrate the microstructural evolution, the 3D morphological microstructure evolution and a 2D cross-section of it are shown over the aging times of 0, 240, and 1100 h in Figure 2.

Comparison of experimental and simulated results after 1100 h of aging: the deviations in the microstructural properties of simulations and experiments observed after 1100 h of aging are consistent with those observed after 240 h. Interestingly, a notable discrepancy is observed in the evolution of the mean nickel particle diameter. In simulations, the mean nickel diameter remains nearly unaltered, increasing slightly from 0.955 μm at 240 h to 0.966 μm at 1100 h. On the contrary, the experimental results show a clear increase from 1.04 to 1.11 μm in the same period (see Table 3). Multiple factors might contribute to this discrepancy. Nickel particles are coarser than GDC particles (0.91 μm compared to 0.59 μm in the pristine state), and the nonpercolating nickel phase accounts for only 22.4% of the total domain volume, compared to 41.4% for GDC and 36.2% for pores. This limited connectivity may hinder coarsening mechanisms as isolated Ni particles present fewer possibilities for coarsening through particle interactions. Furthermore, slight inhomogeneities in the nickel particle distribution across the cell may amplify the deviations between the simulated and experimental microstructures, given the lower volume fractions of nickel. Additionally, the 3D reconstruction and segmentation methods, as well as the diffusivity and energy parameters derived from the Bayesian multiobjective optimization approach, may also introduce some possible associated errors.

3.1.2. Phase-Field Simulations of 860 h Aging: Employing a Preaged (240 h) Ni-GDC Anode as the Input. To further investigate the predictive capability of our phase-field model for simulating the microstructural evolution of Ni-GDC anodes and to examine the influence of local microstructural inhomogeneities on the aging behavior, phase-field simulations are performed using a preaged (240 h) experimental FIB-SEM-reconstructed 3D Ni-GDC anode microstructure as the initial condition. Simulations are performed for an aging duration of 860 h on a preaged (240 h) Ni-GDC anode, effectively resulting in a 1100 h aged microstructure. The resulting microstructural properties are then compared to the experimentally aged microstructure of 1100 h (see Table 3). As shown in Table 3, all microstructural properties show similarities in their evolution behavior between simulations and experiments. In particular, the mean nickel particle diameter increased from 1.04 to 1.08 μm in simulations, compared to an increase from 1.04 to 1.11 μm in experiments. This corresponds to a deviation of about 3%, a significant improvement in accuracy compared to simulations with a pristine microstructure as an initial condition. In conclusion, these results demonstrate that the initial morphological configuration of the Ni particles—and the associated inhomogeneities in the cell—play a role in attaining agreement between experimental and simulated results, in addition to the model's predictive capability. Further quantitative analyses show that the GDC/pore-specific surface area deviates just about 1%, while the total density of the TPBs deviates by 7%. Except for GDC tortuosity deviating 13%, all other microstructural property deviations remain below 7%, which shows a further better agreement with experimental data compared to phase-field simulations initiated with the pristine microstructure. The 3D morphological evolution and a corresponding 2D cross-section of the microstructure over the aging periods of 240, 670, and 1100 h are shown in Figure 3.

All simulated microstructural parameters indicate qualitative agreement and good quantitative accuracy with the experimental results, except for GDC tortuosity. This observed discrepancy between the simulations and experimental results could be attributed to several factors, as outlined below.

- Evolution of degradation kinetics: in experiments, local GDC diffusion values resulting from spatial $p(O_2)$ gradients may deviate from the global value. Furthermore, this work considers and assumes a uniform Ni/GDC wettability over the entire domain due to a lack of experimental findings or data. However, inclusion of a spatially dependent wettability could provide an improved representation of the local GDC redistribution. Additionally, as tortuosity is highly sensitive to local variations in particle connectivity or isolation, as opposed to the volume properties (which are less affected by such local events), minor particle isolation or changes in percolation can alter values significantly.
- Holzer et al.[24] and Sciazko et al.[68] reported in the early stages, coarsening dominates, while in the later stages, an interplay between Ni coarsening and GDC layer formation leads to more complex microstructural evolution. In the current work, a static Ni/GDC wettability is assumed from the initial stage, while the wettability in experiments may evolve dynamically with the local conditions, microstructure redistribution, and over longer aging times.
- Statistical representativeness of the simulated sample volume: variations in tortuosity may partly result from sample-to-sample differences or segmentation inaccuracies. However, the FIB-SEM reconstructions in this study were systematically performed at central anode regions where microstructural homogeneity is highest, thereby minimizing spatial heterogeneity. In our previous work,[48] statistical analysis of four nonoverlapping half-volume subdomains showed CV of only 0−2% for key characteristics, confirming very low variability. As microstructural changes of this magnitude are within the methodological standard deviation reported by Holzer et al.,[24] domain representativeness is unlikely to contribute significantly to the observed discrepancies between GDC tortuosity trends in simulations and experiments.
- Accuracy of the model parameters: the present work employs Ni-GDC parameters derived through an AL framework with Bayesian optimization utilizing experimental microstructures operated at high temperatures of 900 °C in a reducing atmosphere of 50% H_2/50% H_2O under OCV conditions.[48] While this approach provided an optimized parameter set consistent with the available literature, further refinement through multi-objective approaches (e.g., evolutionary algorithms) could improve the accuracy of the parameters. Simulations demonstrate a slower GDC coarsening rate than experiments, as reflected in the slower evolution of the mean particle diameter, suggesting a lower GDC diffusion coefficient used in the model.

3.2. Sensitivity Analyses of Physical Parameters—Influence of Interfacial Energies on Anode Stability.

Investigations into the sensitivity of parameters such as the surface and interfacial energies of the system on long-term stabilities and durabilities of the Ni-GDC SOFC anode microstructure are carried out. Three different thermodynamic equilibrium scenarios are incorporated into the simulation studies through sets of surface and interfacial energy values. The contact angles at the triple point are indirectly controlled via the interfacial energies $\gamma_{\alpha\beta}$ in the current model. The wettability between Ni and YSZ is directly related to the aggregation and coarsening behavior of the Ni particles and affects the long-term stability of SOFCs.[20,32,36] While phase-field studies exist on the influence of the contact angle between Ni and YSZ on microstructural evolutions and thereby properties,[28,30,32,36] systematic phase-field studies of microstructural evolution for the Ni-GDC system where two phases simultaneously evolve are lacking. To investigate these effects, two additional phase-field simulations with the changes in the surface energies of GDC and the interfacial energy of Ni-GDC are carried out, with changes to surface and interfacial energy parameters obtained from an machine learning (ML) Bayesian AL framework. In the literature, both coarsening of nickel and GDC, as well as a smoothing layer of GDC around nickel phenomena, are observed for Ni-GDC systems.[21,24,27] However, the mechanisms responsible for such phenomena still need to be fully understood. Analysis of these morphological evolutions provides additional insight into the underlying mechanisms and the impact on the microstructural properties.

Ni wettability on YSZ is known to significantly influence the stability of the TPB active site and phase contiguity in Ni-YSZ fuel electrode cell anode materials.[30,36] The durability of conventional Ni-YSZ composite electrodes can therefore be improved by controlling the Ni wettability on the YSZ surface. Jiao et al.[20,32,69] systematically investigated the effects of polarization on the morphological evolution of Ni in both SOFC and solid oxide electrolysis cell modes using a patterned Ni film electrode. From their results, it was found that the wettability of Ni on YSZ significantly improved during SOFC operation. This behavior was attributed to the adsorption of oxygen species on the Ni surface, influencing both the surface energy of Ni and the adhesion work at the Ni/YSZ interface. The activity of oxygen adsorbed on the Ni surface was correlated with the equivalent partial pressure of H_2O and equated to an atomic percentage (atom %). With H_2O partial pressure in the range of 0.8−0.994 atm, and just before Ni-oxidation occurs, the Ni contact angle is predicted to decrease sharply from about 110° to below 30°. These experimental results, together with previous studies on Ni-YSZ systems, provide a basis for investigating the influence of the wetting behavior of Ni on the microstructural evolutions of Ni-GDC. Since both Ni and GDC undergo morphological changes during operation, understanding their wetting interactions is essential to the optimization of Ni-GDC anodes and the improvement of their long-term performance.

Here, a contact angle $\theta_\alpha < 90°$ indicates a wetting behavior, while $\theta_\alpha > 90°$ indicates dewetting. The relationships at the triple junction in equilibrium can be expressed as follows:

$$\gamma_{NiGDC} + \gamma_{NiPore}\cos(\theta_{Ni}) + \gamma_{GDCPore}\cos(\theta_{GDC}) = 0 \qquad (22)$$

$$\gamma_{GDCPore}\sin(\theta_{GDC}) = \gamma_{NiPore}\sin(\theta_{Ni}) \qquad (23)$$

Here, γ_{NiPore}, $\gamma_{GDCPore}$, and γ_{NiGDC} denote surface energies of Ni and GDC with the pore phase and the interfacial energy between Ni and GDC, respectively. θ_{Ni} and θ_{GDC} represent the contact angles of the nickel and GDC phases, respectively. Surface and interfacial energies obtained from Bayesian AL ML studies are γ_{NiGDC}, γ_{NiPore}, and $\gamma_{GDCPore}$ as 2.43, 2.1, and 1.43 J m^{-2}, respectively,[48] and the computed equilibrium contact angles for Ni, GDC, and the pore phase in this configuration are θ_{Ni}−θ_{GDC}−θ_{Pore} as 144°−121°−95°, respectively. We selected the other two contact angle configurations based on two main criteria. First, the variation in the angles studied needs to be sufficiently large to ensure that observed trends in the simulations could be attributed to changes in the relevant contact angle configurations. Second, both scenarios of Ni and GDC wetting in the Ni-GDC system needed to be covered. A lower bound of 60° is selected for nickel contact angle θ_{Ni}, consistent with reported experimental values in Ni-YSZ systems under polarization.[20] The other two configurations of contact angles are as follows: θ_{Ni}−θ_{GDC}−θ_{Pore} as 60°−152°−148° and 144°−60°−156°. The presented simulation studies provide meaningful insights into the potential for mitigating anode degradation through optimized contact angles. Investigations into the practical feasibility of such contact angle configurations within the Ni-GDC system, however, are beyond the scope of this manuscript. Based on eqs 22 and 23, the calculated equivalent contact angles of Ni, GDC, and pore based on the given surface and interfacial energies in the Ni-GDC system are summarized in Table 4. A sum of all three phase angles of 360° was ensured in the calculations.

Table 4. Equilibrium Contact Angles at Triple Junctions Corresponding to Three Different Sets of Specified Interfacial Energies[a]

γ_{NiGDC} (J m^{-2})	γ_{NiPore} (J m^{-2})	$\gamma_{GDCPore}$ (J m^{-2})	θ_{Ni} (deg)	θ_{GDC} (deg)	θ_{Pore} (deg)
2.43	2.1	1.43	144	121	95
2.43	2.1	3.92	60	152	148
0.98	2.1	1.43	144	60	156

[a] The values in the first row γ_{NiGDC}, γ_{NiPore}, and $\gamma_{GDCPore}$ (2.43, 2.10, and 1.43 J m^{-2}) correspond to the results of our previous work,[48] whereas second- and third-row values represent the assumed and modified surface energy of GDC and interfacial energy of Ni/GDC to obtain a target contact angle of 60° for both Ni and GDC.

3.2.1. Effect of Interfacial Energies on Morphological Evolutions: 2D Analysis. The complexity of the 3D Ni-GDC anode microstructure and its evolution present difficulty in gaining a clear understanding of the role of interfacial energies and associated morphological evolutions. Therefore, for a mechanistic understanding of the influence of interfacial energies, an analysis is conducted using a simplified 2D two-particle system consisting of Ni and GDC particles. Phase-field simulations are performed using three triple junction equilibrium contact angle scenarios (as presented in Table 4), representing distinct surface and interfacial energy conditions. Encompassing dewetting to wetting interactions of both nickel and GDC, these scenarios provide a detailed understanding of the interfacial energies governing the morphological evolution of Ni and GDC.

The initial system consists of two equal-sized, adjacent rectangular nickel and GDC particles in contact at a common interface and aligned at right angles. To ensure general applicability, all quantities are expressed in an arbitrary unit system. The energy unit is defined as $\mathrm{u}_E \equiv \lambda_E$ J, where λ_E is a dimensionless prefactor and J denotes joules. Similarly, units of length and time are defined as $\mathrm{u}_l \equiv \lambda_l$ m and $\mathrm{u}_t \equiv \lambda_t$ s, respectively, where the dimensionless prefactors λ_l and λ_t correspond to their SI equivalents. The simulation domain consists of a grid with a width of $N_x = 200$ cells and a height of $N_y = 200$ cells. Zero flux boundary conditions are applied at the domain boundaries, which are treated as insulating. The spatial discretization is set to $\Delta x = \Delta y = 1\ \mathrm{u}_l$. Both nickel and GDC components are assumed to have the same diffusivity along their surfaces and at their mutual interfaces. This assumption of assigning equal diffusivity values to the nickel and GDC components allows for faster convergence to the thermodynamic equilibrium state. Here, the primary objective is to study the final morphological configuration of the system at equilibrium. Consequently, equal chemical surface and interface mobilities of $M_{\mathrm{Ni}}^{NiPore} = M_{\mathrm{Ni}}^{NiGDC} = M_{\mathrm{GDC}}^{GDCPore} = M_{\mathrm{GDC}}^{NiGDC} = 0.1\ \mathrm{u}_l^6/(\mathrm{u}_E{\cdot}\mathrm{u}_t)$ are assigned, whereby equal rates of mass transport via surface diffusion of nickel and GDC and interface diffusion between nickel and GDC are ensured. The interfacial energy values corresponding to the three contact angle configurations considered in the model are given as follows: (γ_{NiGDC}, γ_{NiPore}, and $\gamma_{GDCPore}$) = (1.15, 1.0, 0.68), (1.15, 1.0, 1.87), and (0.47, 1.0, 0.68). These values define the relative energetics that drive morphological evolution in each scenario. Simulations are performed for a sufficiently long time to ensure that only negligible changes are observed in later phases, corresponding to an equilibrated system.

Figure 4a shows the initial configuration of Ni and GDC, two solid particles in contact with each other. Figure 4b−d depicts the morphological evolution at equilibrium under different interfacial energy conditions, simulated by the phase-field model. In Figure 4b, the contact angles for nickel, GDC, and the pore phase are 144°, 121°, and 95°, respectively. Due to a higher interfacial energy, the system evolves by minimizing the Ni/GDC interface, thereby evolving in a thermodynamically consistent manner to reduce the total energy of the system. Consequently, this configuration represents a dewetting scenario, where Ni and GDC display a limited chemical affinity for each other. As shown in Figure 4c, the contact angles are 60°, 152°, and 148° for nickel, GDC, and the pore phases, respectively. Here, the system primarily reduces the surface area of the GDC as this is energetically unfavorable. This results in a wetting configuration in which Ni tends to spread around the GDC particle. In Figure 4d, the contact angles for nickel, GDC, and the pore phase are 144°, 60°, and 156°, respectively, indicating that the system minimizes the surface of nickel due to its relatively high surface energy. This results in a wetting configuration of GDC around the Ni particle. Simulated contact angles are in good agreement with

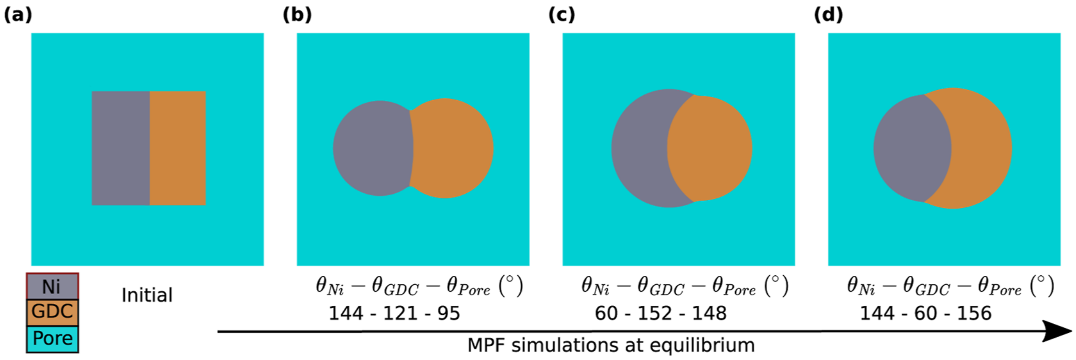

Figure 4. Morphological evolutions of (a) initial two adjoining nickel and GDC particles contacting a common interface at right angles. (b−d) Morphological evolution at equilibrium by the phase-field simulations using the same kinetic coefficients and paths but with different sets of thermodynamic equilibrium contact angles θ_{Ni}−θ_{GDC}−θ_{Pore} as 144°−121°−95°, 60°−152°−148°, and 144°−60°−156°, respectively.

Table 5. Microstructural Characteristic Properties over the Aging of Three Simulations with Distinct Configurations of Contact Angles

θ_{Ni}−θ_{GDC}−θ_{Pore} (deg)	t (h)	τ_{GDC}	τ_{Pore}	d_{Ni} (μm)	d_{GDC} (μm)	d_{Pore} (μm)	l_{TPB} (μm^{-2})	$A_{Ni/Pore}$ (μm^{-1})	$A_{GDC/Pore}$ (μm^{-1})	$A_{Ni/GDC}$ (μm^{-1})
144−121−95	0	2.573	2.573	0.913	0.588	0.601	1.82	0.371	1.5	0.672
144−121−95	200	2.519	2.570	0.956	0.603	0.63	1.529	0.314	1.447	0.616
144−121−95	2000	2.388	2.605	0.968	0.625	0.678	1.364	0.285	1.367	0.605
60−152−148	0	2.573	2.573	0.913	0.588	0.601	1.82	0.371	1.5	0.672
60−152−148	200	2.523	2.893	0.716	0.601	0.75	1.67	0.335	1.125	0.936
60−152−148	2000	2.367	3.386	0.667	0.619	0.857	1.429	0.288	1.002	0.978
144−60−156	0	2.573	2.573	0.913	0.588	0.601	1.82	0.371	1.5	0.672
144−60−156	200	2.517	2.678	0.867	0.599	0.676	1.531	0.298	1.334	0.754
144−60−156	2000	2.364	2.831	0.857	0.609	0.739	1.329	0.262	1.245	0.779

the values of the interfacial energy, and the corresponding contact angle calculations are given in Table 4. Thus, the phase-field simulations accurately incorporate the prescribed interfacial energy and effectively capture the morphological evolution driven by the minimization of the interfacial energy.

3.2.2. Effects of Interface Energies on Morphological Evolutions: 3D Analysis of FIB-SEM-Reconstructed Experimental Ni-GDC SOFC Anode Microstructures. Phase-field aging simulations are conducted on a FIB-SEM-reconstructed pristine 3D Ni-GDC anode microstructure, incorporating three different contact angle scenarios. These simulations aim to analyze the influence of different contact angle configurations on the degradation of microstructural properties. The characteristic microstructural properties of these simulations for aging times of 0 h, 200 h, and 2000 h are presented in Table 5. It can be seen that the contact angle relationships significantly affect the kinetics of particle growth, structural tortuosity, and interfacial properties. Furthermore, contact angles also influence the density of the total TPBs. Microstructural changes are directly related to the electrochemical performance and gas transport mechanisms and thus to the long-term stability of SOFC anodes. A detailed analysis of the correlations between contact angles and microstructural properties allows for a targeted optimization of operating conditions and interface energies, whereby both the durability and efficiency of SOFCs can be effectively improved. The morphological evolution of the 3D Ni-GDC anode microstructure and their phases from the initial microstructures after an aging time of 2000h for the three scenarios of contact angle are shown in Figure 5. For clarity and ease of reference, we categorize the three configurations as follows: high contact angle configuration: θ_{Ni}−θ_{GDC}−θ_{Pore} = 144°−121°−95°; low Ni contact angle configuration: θ_{Ni}−θ_{GDC}−θ_{Pore} = 60°−152°−148°; low GDC contact angle configuration: θ_{Ni}−θ_{GDC}−θ_{Pore} = 144°−60°−156°.

Figure 6a shows the evolution of the nickel mean particle diameter for three different contact angle configurations. Among these, the high contact angle configuration exhibits an increase in mean diameter of about 6% over an aging period of 2000 h. In contrast, the low Ni contact angle configuration results in a significant decrease in the mean diameter by 27%. Lastly, the low GDC contact angle configuration also shows a decrease in mean diameter, though it is more moderate at about 6%. A similar decline in nickel mean particle diameter is also reported in phase-field studies by Davis et al.[30] at lower contact angles of nickel. Despite these quantitative differences, all three configurations display a similar qualitative trend of an initial period of accelerated growth or decline in mean particle diameter for nickel, consistent with previous phase-field studies on Ni-YSZ systems.[47] From these results, it can be seen that interfacial energies and, respectively, contact angle conditions strongly control the coarsening behavior. Low contact angle configurations, indicative of improved wetting, promote a coating-like microstructure (as illustrated in Figure 5c for nickel), which contrasts with the morphology observed at the high contact angle configuration. The significant reduction in mean nickel diameter for the low Ni contact angle configuration is a result of the increased Ni/GDC interfacial area due to the nickel coating around the GDC particles. Such evolution is evident from the increase in Ni/GDC interface area density from 0.672 to 0.978 μm^{-1} (see Table 5), thereby resulting in a lower total energy of the system. Furthermore, this wetting behavior contributes to a further reduction in the GDC surface area density, associated with a higher energy, from 1.5 to 1.002 μm^{-1}, along with a coarsening mechanism of the GDC particles to minimize the surface area. In the utilized

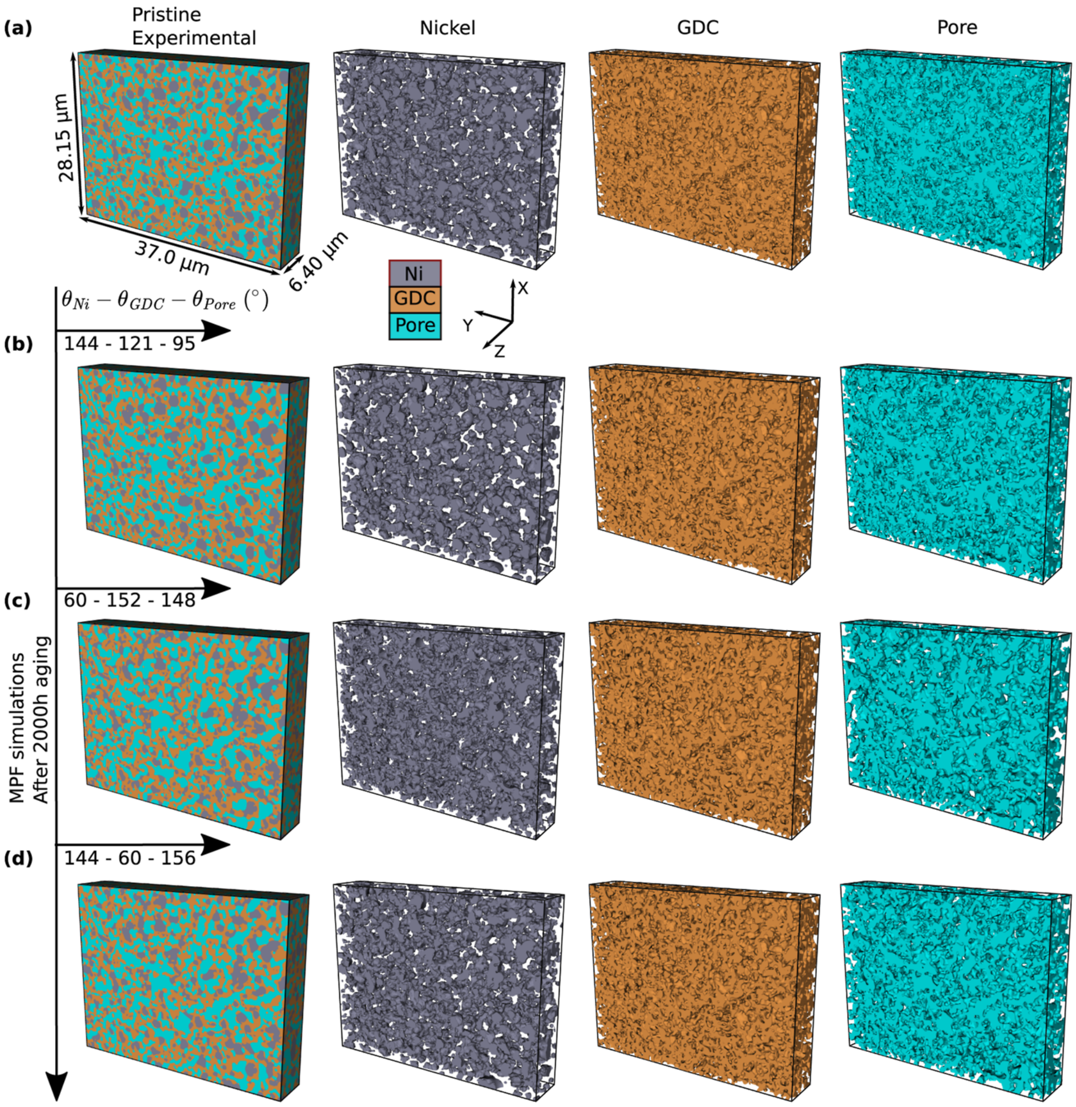

Figure 5. Morphological evolution of the (a) initial pristine 3D Ni-GDC anode microstructure and constituent phases over 2000 h of aging, simulated for (b−d) three distinct contact angle configurations using the MPF method.

morphology of the 3D Ni-GDC anode for the contact angle sensitivity studies, where volume fractions of nickel are 22.44% and the nickel particles are nonpercolated, the coating of nickel around GDC particles at nickel/GDC interfaces predominated over the coarsening of nickel particle interactions. This results in a pronounced decrease in the mean particle diameter of nickel from the initial configuration over aging for smaller contact angles. The complex interplay between the mechanisms of Ni wettability enhancement at Ni/GDC interfaces and the coarsening of Ni particles ultimately determines the morphological evolution of nickel as observed in this configuration. The low GDC contact angle configuration exhibits a moderate decrease in the mean Ni particle diameter, while including a Ni contact angle of 144°. Here, the low GDC contact angle (60°) promotes the formation of a continuous GDC layer around Ni, suppressing Ni coarsening. Also in this configuration, the Ni/GDC interfacial energy (0.98 J m^{-2}) is lower than the surface energies of Ni (2.1 J m^{-2}) and GDC (1.43 J m^{-2}), which favors an increase of the Ni/GDC interfacial area, leading to a reduction of the total energy of the system. Thus, the observed moderate decrease in the mean Ni particle diameter is not solely due to the Ni contact angle, but rather to the coupled evolution of the Ni and GDC phases, with wetting by GDC strongly influencing Ni stability and particle growth. Holzer et al.[24] reported similar observations of enhanced GDC wetting in humid environments covering Ni grains, suppressed growth over the long run, and even negative growth.

As shown in Figure 6b, the evolution of the mean particle diameter (d_{50}) of GDC exhibits distinct growth patterns across the three contact angle configurations. As expected, the high contact angle configuration resulted in more pronounced GDC particle growth than configurations with low contact angles of Ni and GDC. Among the low contact angle configurations, the low GDC contact angle configuration suppressed GDC particle growth more. This can be attributed to the higher volume fraction of GDC (41.38%) compared to nickel (22.44%) and the smaller mean diameter of GDC particles (0.59 μm vs 0.91 μm in nickel) in the initial microstructure. The morphological evolution of nickel can be observed rather quickly compared to GDC owing to the significantly higher diffusivities of nickel compared to GDC (about 5 orders of magnitude).[48] As reported by Zekri et al.,[21] the formation of a GDC coating

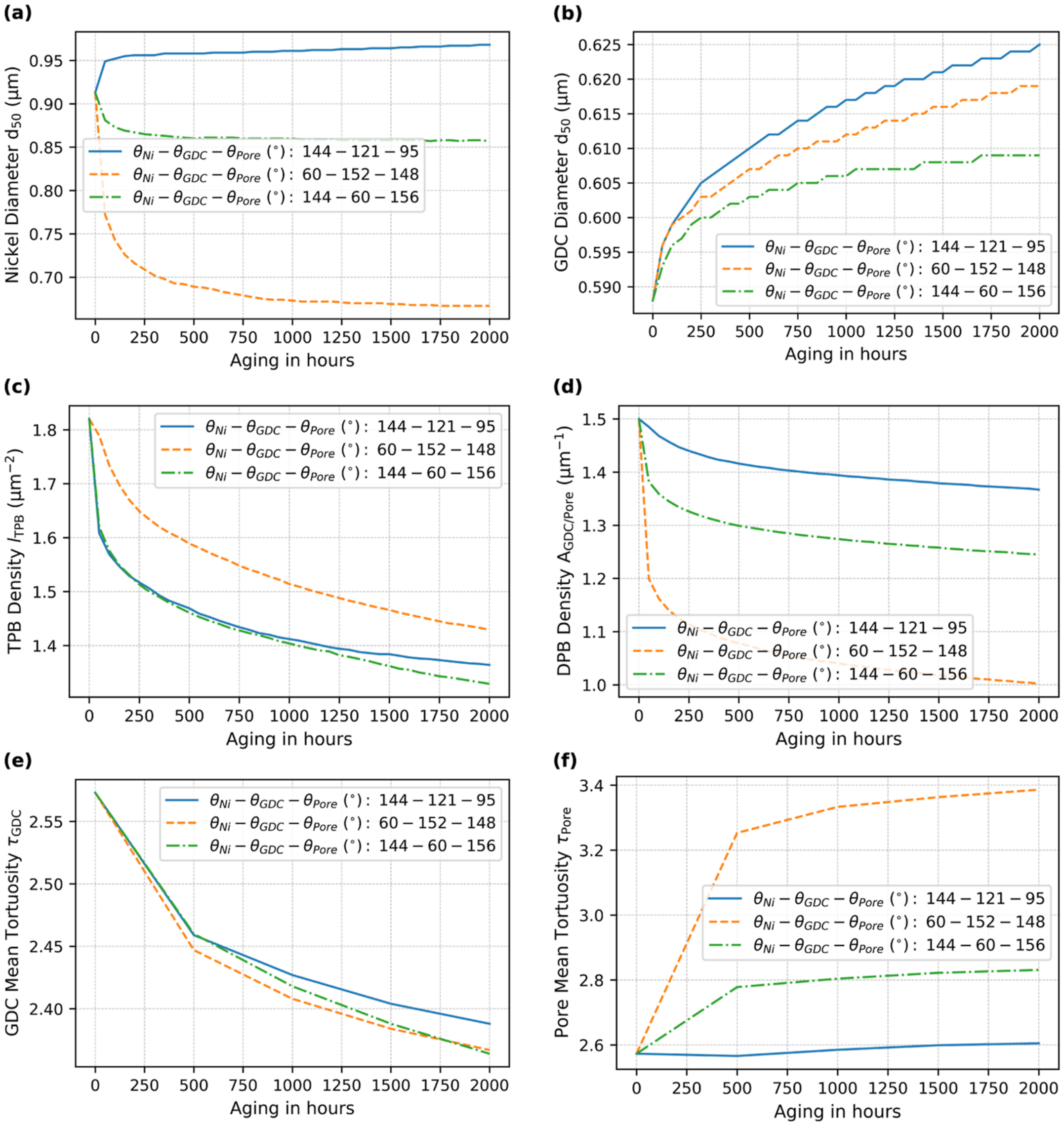

Figure 6. Microstructural properties evolution over the aging period of 2000 h for three distinct configurations of contact angles in the MPF simulations: (a,b) mean diameter of nickel and GDC, (c) total TPB density, (d) DPB density, (e,f) mean tortuosities of GDC and pore.

around nickel can be observed only after longer operating hours.

To analyze the distribution of the total three-phase boundary sites, the evolution of TPB density over the 2000 h aging period is presented in Figure 6c. Across all contact angle configurations, TPB density undergoes substantial degradation, decreasing from an initial value of approximately 1.82 μm^{-2} to a range of 1.33−1.43 μm^{-2}, corresponding to an overall reduction of 21% to 27%. This decline indicates a significant loss of electrochemically active sites, directly affecting the cell performance. Among the tested configurations, the low Ni contact angle configuration exhibits the most favorable TPB retention, with the smallest overall reduction over the 2000 h aging period. The observed results can be attributed to the stronger suppression of nickel coarsening and the rapid formation of a nickel layer around GDC particles due to its higher diffusivity. This layer inhibits GDC evolution, thereby preserving interfacial pores more effectively than in other configurations,[69] ultimately leading to higher TPB densities. Conversely, the high contact angle configuration initially exhibits a TPB degradation rate similar to that of the configuration with a low GDC contact angle. However, at longer aging times, the reduction in the TPB density is less severe than in the low GDC contact angle configuration. This trend aligns with previous findings by Davis et al.,[30] which suggest that high-contact-angle systems, characterized by lower wettability, promote the formation of closed-loop TPBs, stabilizing the TPB density over time. The most pronounced TPB degradation is observed in the low GDC contact angle configuration, which experiences a sharp decline within the first 250 h, followed by a more gradual reduction. Theoretical considerations by Jiao et al.[69] indicate that systems with initially high TPB density, such as Ni-YSZ composites, undergo rapid TPB degradation at early stages due to the elimination of interfacial pores via coalescence. Similarly, in the Ni-GDC system, the wetting behavior of GDC at Ni/GDC interfaces gradually reduces interfacial pores over longer aging times, owing to the slower diffusion coefficients of GDC, thereby decreasing TPB density. While GDC layer formation might suppress nickel coarsening, it is unlikely to prevent early stage degradation due to comparatively lower diffusivity values of GDC. However, at extended operating times, this coating effect could mitigate further coarsening of nickel and stabilize the TPB densities.

These findings underscore the critical role of interfacial energies in shaping individual phase morphologies and the stability of three-phase junctions, which are essential for electrochemical activity and performance. Notably, a low Ni contact angle configuration contributes to enhanced microstructural stability by preserving TPB density over long-term operation of 2000 h. Nevertheless, the overall variation in TPB degradation across the tested configurations remains relatively small—ranging from approximately 2% to 6% at 2000 h—compared to the initial degradation of 21% to 27%. The competing mechanisms of Ni and GDC coarsening, coupled with wetting and dewetting conditions at Ni/GDC interfaces, add complexity to the morphological evolution. Further quantitative investigations into large-scale simulations of dewetting and wetting behavior, Ni and GDC coating-like formation around particles, and their impact on microstructural properties are necessary to improve composite SOC electrodes for enhanced durability and performance.

Figure 6d shows the evolution of the DPB density over the 2000h aging period to estimate the distribution of total double-phase boundaries. In Ni-GDC systems, DPBs provide additional electrochemical reaction sites owing to the mixed ionic and electronic conductivities of GDC. Over the aging period, the DPB density shows a monotonic decline across all contact angle configurations, decreasing from an initial value of about 1.5 $\mu\mathrm{m}^{-1}$ to a range of 1.0−1.37 $\mu\mathrm{m}^{-1}$, corresponding to an overall reduction of 9−33%. Among the configurations investigated, the high contact angle configuration exhibits the highest stability of the DPB distribution with the least overall reduction in GDC/pore interface density over the aging period. Here, the coarsening mechanism of the GDC particles mainly contributes to the reduction of the total GDC surface area. In contrast, the low Ni contact angle configuration experiences the most significant degradation, attributed to the formation of a Ni layer around the GDC particles. This layer effectively reduces the exposed GDC surface area, leading to a more pronounced decrease in the DPB density. The low GDC contact angle configuration shows a moderate decrease in the number of DPBs among the three configurations.

Figure 6e shows the evolution of the GDC tortuosity across contact angle configurations. The tortuosity of the GDC phase is a key factor influencing oxygen ion and electron transport within the anode as higher tortuosity values indicate more restricted conduction pathways. Elevated tortuosity values are also associated with an increased likelihood of phase discontinuities due to the formation of islands, thus rendering these values a potential stability indicator for anode operation. Over the aging period, GDC tortuosity changes remain relatively minor, with values decreasing across all configurations from approximately 2.57 to 2.36. This modest decline suggests that ion and electron transport pathways remain largely stable over aging. However, for the low GDC contact angle configuration, the initial tortuosity value decreases relatively more, suggesting GDC wettability can improve electron and ion conduction over long-term operation. In Ni-YSZ systems, phase-field simulations by Hoffrogge et al.[36] reported improved nickel tortuosity values at lower contact angles of nickel. Pore tortuosity is a critical parameter for gas transport within the anode microstructure, with larger values indicating more convoluted diffusion pathways and potentially limiting the availability of reactants at electrochemically active sites. The evolution of pore tortuosity, averaged over three orthogonal directions for 2000 h of aging, is shown in Figure 6f. Among the tested configurations, the high contact angle configuration exhibits the most stable behavior with negligible changes in pore tortuosity during aging. This observation is consistent with phase-field studies by Chen et al.,[28] indicating that prolonged coarsening in Ni-YSZ systems can have a positive effect on gas transport in the pore phase. Given the moderate coarsening in the microstructures studied, the observed trend in tortuosity is consistent with the previous findings. Conversely, the low Ni contact angle configuration shows a pronounced increase in pore tortuosity, elevating from 2.57 to 3.39—a 32% increase. This deterioration can be attributed to the formation of a continuous nickel layer, obstructing and altering the pore phase pathways. Similarly, the low GDC contact angle configuration exhibits a moderate increase in the tortuosity. Overall, high contact angles appear to mitigate pore constriction and suppress tortuosity value growth, thereby enhancing the reactant diffusivity.

The high contact angle configuration exhibits the most severe degradation, characterized by significant nickel and GDC coarsening and substantial loss of TPB sites, while the DPB density remains relatively stable. In contrast, the low Ni contact angle configuration inhibits nickel coarsening and allows moderate GDC growth, resulting in a lower TPB density degradation at the expense of a higher DPB density degradation. The low GDC contact angle configuration stabilizes the GDC particle size but exhibits pronounced TPBs degradation and a moderate loss of DPBs, with the low diffusion coefficients of GDC playing a dominant role in degradation over longer operating hours. Each configuration is characterized by trade-offs between TPBs, DPBs, and tortuosity, complicating the determination of optimal contact angle conditions. The microstructural properties obtained from phase-field simulations, such as tortuosity, TPB, and DPB densities, can be integrated into transmission line models for Ni-GDC anodes to predict the temporal evolution of the polarization resistance and determine the optimal contact angle configuration.

The current model is primarily applicable to Ni-GDC or Ni-YSZ anodes subjected to high-temperature, open-circuit thermal aging conditions, where the microstructural evolutions are dominated by coarsening mechanisms. In the current work, model validity is demonstrated by employing reconstructed electrode microstructures from a cell aged under purely thermal humidified OCV conditions in a symmetrical configuration. The model explicitly incorporates interfacial energies and diffusion coefficients along surfaces and interfaces and thus accounts for mass transport along grain boundaries, surfaces, and interfaces. Anisotropic interfacial energies and diffusion coefficients can certainly be included in the current model, but their inclusion is limited by the high computational cost associated with large-scale simulations of larger domains. In thick anodes, $p(\mathrm{O}_2)$ gradients can lead to nonuniform wettability along the thickness, as reported in the literature for Ni-YSZ systems.[70] Such effects could also be relevant for Ni-GDC systems. The present work assumes uniform wettability across the entire domain due to the lack of experimental findings or data on the wetting angle distribution in Ni-GDC anodes. However, the model can incorporate spatially dependent wettability upon the availability of such results or data, allowing for a more comprehensive understanding of the Ni-GDC redistribution and degradation. While the model can

https://doi.org/10.1021/acsaem.5c02218

easily be extended to include additional contributions from volume diffusion, additional degradation mechanisms such as evaporation−condensation processes and GDC migration under polarization are not yet included in the model. All of these additional contributions require experimentally measured input parameters under operating conditions and precise calibration. Further research is needed to uncover the mechanisms that drive these morphological changes.

4. CONCLUSION

In this work, the coarsening behavior of Ni and GDC in FIB-SEM-reconstructed 3D Ni-GDC SOFC anodes was simulated using a multiphase-field model under operating conditions of Ni-GDC at a temperature of 900 °C with a gas composition of 50% H_2/50% H_2O. Both surface diffusion of nickel and GDC components and their interfacial diffusion along the Ni/GDC interface were included in the model. By using both pristine and preaged microstructures, the model's predictive capability under various initial conditions was evaluated. Validation results included the evolution of the mean particle size, TPB density, tortuosity, and specific surface areas. Validation with both pristine and preaged microstructures showed good agreement with experimental results for all microstructural properties, except for GDC tortuosity, with preaged microstructures showing further improved accuracy. Several factors potentially contributing to discrepancies between the simulation and experimental results, particularly GDC tortuosity, are discussed. The influence of surface and interfacial energies on the degradation of Ni-GDC anodes, considering three thermodynamic equilibrium scenarios defined by a set of interfacial energies, highlighted wettability as a key factor in the microstructural degradation pathways in Ni-GDC anodes. Initial 2D simulations demonstrated the role of interfacial energies in governing the morphological evolution of Ni and GDC. Subsequent 3D phase-field simulations on pristine Ni-GDC microstructures over 2000 h of aging revealed that the wettability of Ni and GDC significantly influences the balance between TPB and DPB evolutions. A low Ni contact angle primarily mitigates Ni coarsening, whereas a low GDC contact angle influences Ni's long-term stability. Each investigated configuration revealed trade-offs among key microstructural properties such as TPBs, DPBs, and tortuosity, complicating the identification of an optimal contact angle condition. With the predictive capability of our phase-field model for Ni-GDC anode degradation validated, future work will focus on integrating phase-field simulations, electrochemical modeling, and synthetic microstructures with tailored volume fractions and particle sizes of Ni and GDC. This combined approach intends to optimize the microstructural design for improved performance and durability of Ni-GDC anodes.

■ ASSOCIATED CONTENT

Data Availability Statement

Data will be made available on request.

■ AUTHOR INFORMATION

Corresponding Authors

R. K. Jeela − *Institute of Digital Materials Science (IDM), Karlsruhe University of Applied Sciences, 76133 Karlsruhe, Germany; Institute for Applied Materials—Microstructure Modelling and Simulation (IAM-MMS), Karlsruhe Institute of Technology (KIT), 76131 Karlsruhe, Germany;* orcid.org/0009-0003-6995-8524; Email: Ravi_Kumar.Jeela@hs-karlsruhe.de

D. Schneider − *Institute of Digital Materials Science (IDM), Karlsruhe University of Applied Sciences, 76133 Karlsruhe, Germany; Institute for Applied Materials—Microstructure Modelling and Simulation (IAM-MMS), Karlsruhe Institute of Technology (KIT), 76131 Karlsruhe, Germany; Institute of Nanotechnology—Microstructure Simulations (INT-MSS), Karlsruhe Institute of Technology (KIT), 76344 Eggenstein-Leopoldshafen, Germany;* Email: daniel.schneider@kit.edu

Authors

M. Ahmad − *Institute of Digital Materials Science (IDM), Karlsruhe University of Applied Sciences, 76133 Karlsruhe, Germany*

M. Wieler − *Computational Materials Engineering (CR/ATC1), Robert Bosch GmbH, 71272 Renningen, Germany;* orcid.org/0000-0002-6328-0316

Y. Liu − *Institute for Applied Materials—Electrochemical Technologies (IAM-ET), Karlsruhe Institute of Technology (KIT), 76131 Karlsruhe, Germany*

M. Juckel − *Institute of Energy Materials and Devices, Materials Synthesis and Processing (IMD-2), Forschungszentrum Jülich GmbH, 52428 Jülich, Germany*

A. Weber − *Institute for Applied Materials—Electrochemical Technologies (IAM-ET), Karlsruhe Institute of Technology (KIT), 76131 Karlsruhe, Germany*

N. H. Menzler − *Institute of Energy Materials and Devices, Materials Synthesis and Processing (IMD-2), Forschungszentrum Jülich GmbH, 52428 Jülich, Germany;* orcid.org/0000-0001-7091-0980

B. Nestler − *Institute of Digital Materials Science (IDM), Karlsruhe University of Applied Sciences, 76133 Karlsruhe, Germany; Institute for Applied Materials—Microstructure Modelling and Simulation (IAM-MMS), Karlsruhe Institute of Technology (KIT), 76131 Karlsruhe, Germany; Institute of Nanotechnology—Microstructure Simulations (INT-MSS), Karlsruhe Institute of Technology (KIT), 76344 Eggenstein-Leopoldshafen, Germany*

Complete contact information is available at: https://pubs.acs.org/10.1021/acsaem.5c02218

Author Contributions

R.K. Jeela: conceptualization of this study, methodology, software, visualization, validation, writing—original draft, and writing—review and editing. **M. Ahmad:** software and validation. **M. Wieler:** funding acquisition, resources, and conceptualization. **Y. Liu:** writing—original draft. **M. Juckel:** writing—original draft. **D. Schneider:** methodology, project administration, conceptualization, and writing—review and editing. **A. Weber:** funding acquisition, project administration, and writing—review and editing. **N. H. Menzler:** funding acquisition, resources, conceptualization, and writing—review and editing. **B. Nestler:** funding acquisition, project administration, conceptualization, supervision, and writing—review and editing.

Notes

The authors declare no competing financial interest.

■ ACKNOWLEDGMENTS

Most of this work was computed on the idm-hpc03, HPC cluster of the Institute of Digital Materials Science (IDM), Karlsruhe University of Applied Sciences. The authors acknowledge the assistance of the State of Baden-Württemberg through bwHPC. The authors gratefully acknowledge funding from the German Federal Ministry of Education and Research (BMBF) for the WirLebenSOFC project (funding code 03SF0622D) and from the German Research Foundation (DFG) for the project Ceria-based Cathodes for High Performance Electrolysis Cells (project number 467256728). Additional support is provided by the Helmholtz Association, programme "Materials Science and Engineering (MSE)", no. 43.31.01, which is gratefully acknowledged. The authors would like to thank Dr. Paul W. Hoffrogge for valuable insights and helpful discussions during this research.

■ REFERENCES

(1) Ormerod, R. M. Solid oxide fuel cells. *Chem. Soc. Rev.* **2003**, *32*, 17−28.

(2) Wachsman, E. D.; Lee, K. T. Lowering the temperature of solid oxide fuel cells. *Science* **2011**, *334*, 935−939.

(3) Stambouli, A. B.; Traversa, E. Fuel cells, an alternative to standard sources of energy. *Renewable Sustainable Energy Rev.* **2002**, *6*, 295−304.

(4) Wang, C.; Nehrir, M. H. Distributed generation applications of fuel cells. In *2006 power systems conference: advanced metering, protection, control, communication, and distributed Resources*; IEEE: Clemson, SC, USA, 2006, pp 244−248.

(5) Steele, B. C. H.; Heinzel, A. Materials for Fuel-Cell Technologies. *Nature* **2001**, *414*, 345−352.

(6) Samson, A. J.; Søgaard, M.; Hendriksen, P. V. Model for solid oxide fuel cell cathodes prepared by infiltration. *Electrochim. Acta* **2017**, *229*, 73−95.

(7) Zhang, J.; Lenser, C.; Menzler, N. H.; Guillon, O. Comparison of solid oxide fuel cell (SOFC) electrolyte materials for operation at 500 °C. *Solid State Ionics* **2020**, *344*, 115138.

(8) Jaiswal, N.; Tanwar, K.; Suman, R.; Kumar, D.; Upadhyay, S.; Parkash, O. A brief review on ceria based solid electrolytes for solid oxide fuel cells. *J. Alloys Compd.* **2019**, *781*, 984−1005.

(9) Zhang, C.; Grass, M. E.; McDaniel, A. H.; DeCaluwe, S. C.; Gabaly, F. E.; Liu, Z.; McCarty, K. F.; Farrow, R. L.; Linne, M. A.; Hussain, Z.; Jackson, G. S.; Bluhm, H.; Eichhorn, B. W. Measuring fundamental properties in operating solid oxide electrochemical cells by using in situ X-ray photoelectron spectroscopy. *Nat. Mater.* **2010**, *9*, 944−949.

(10) Chueh, W. C.; Hao, Y.; Jung, W.; Haile, S. M. High electrochemical activity of the oxide phase in model ceria-Pt and ceria-Ni composite anodes. *Nat. Mater.* **2012**, *11*, 155−161.

(11) Chueh, W. C.; Haile, S. M. Electrochemical studies of capacitance in cerium oxide thin films and its relationship to anionic and electronic defect densities. *Phys. Chem. Chem. Phys.* **2009**, *11*, 8144−8148.

(12) Haga, K.; Adachi, S.; Shiratori, Y.; Itoh, K.; Sasaki, K. Poisoning of SOFC anodes by various fuel impurities. *Solid State Ionics* **2008**, *179*, 1427−1431.

(13) Klein, J.-M.; Georges, S.; Bultel, Y. Modeling of a SOFC fueled by methane: anode barrier to allow gradual internal reforming without coking. *J. Electrochem. Soc.* **2008**, *155*, B333.

(14) Iwanschitz, B.; Sfeir, J.; Mai, A.; Schütze, M. Degradation of SOFC anodes upon redox cycling: a comparison between Ni/YSZ and Ni/CGO. *J. Electrochem. Soc.* **2010**, *157*, B269−B278.

(15) Klemensø, T.; Mogensen, M. Ni−YSZ solid oxide fuel cell anode behavior upon redox cycling based on electrical characterization. *J. Am. Ceram. Soc.* **2007**, *90*, 3582−3588.

(16) Sarantaridis, D.; Atkinson, A. Redox cycling of Ni-based solid oxide fuel cell anodes: a review. *Fuel cells* **2007**, *7*, 246−258.

(17) Lee, J.-H.; Moon, H.; Lee, H.-W.; Kim, J.; Kim, J.-D.; Yoon, K.-H. Quantitative analysis of microstructure and its related electrical property of SOFC anode, Ni−YSZ cermet. *Solid State Ionics* **2002**, *148*, 15−26.

(18) Faes, A.; Hessler-Wyser, A.; Presvytes, D.; Vayenas, C.; Herle, J. V. Nickel−zirconia anode degradation and triple phase boundary quantification from microstructural analysis. *Fuel cells* **2009**, *9*, 841−851.

(19) Iwanschitz, B.; Holzer, L.; Mai, A.; Schütze, M. Nickel agglomeration in solid oxide fuel cells: The influence of temperature. *Solid State Ionics* **2012**, *211*, 69−73.

(20) Jiao, Z.; Shikazono, N. Study on the effects of polarization on local morphological change of nickel at active three-phase-boundary using patterned nickel-film electrode in solid oxide fuel cell anode. *Acta Mater.* **2017**, *135*, 124−131.

(21) Zekri, A.; Knipper, M.; Parisi, J.; Plaggenborg, T. Microstructure degradation of Ni/CGO anodes for solid oxide fuel cells after long operation time using 3D reconstructions by FIB tomography. *Phys. Chem. Chem. Phys.* **2017**, *19*, 13767−13777.

(22) Fang, Q.; Frey, C. E.; Menzler, N. H.; Blum, L. Electrochemical performance and preliminary post-mortem analysis of a solid oxide cell stack with 20,000 h of operation. *J. Electrochem. Soc.* **2018**, *165*, F38−F45.

(23) Trini, M.; Hauch, A.; De Angelis, S.; Tong, X.; Hendriksen, P. V.; Chen, M. Comparison of microstructural evolution of fuel electrodes in solid oxide fuel cells and electrolysis cells. *J. Power Sources* **2020**, *450*, 227599.

(24) Holzer, L.; Iwanschitz, B.; Hocker, T.; Münch, B.; Prestat, M.; Wiedenmann, D.; Vogt, U.; Holtappels, P.; Sfeir, J.; Mai, A.; Graule, T. Microstructure degradation of cermet anodes for solid oxide fuel cells: Quantification of nickel grain growth in dry and in humid atmospheres. *J. Power Sources* **2011**, *196*, 1279−1294.

(25) Ouyang, Z.; Komatsu, Y.; Sciazko, A.; Onishi, J.; Nishimura, K.; Shikazono, N. Operando observations of active three phase boundary of patterned nickel-Yttria stabilized zirconia electrode in solid oxide cell. *J. Power Sources* **2022**, *529*, 231228.

(26) Komatsu, Y.; Sciazko, A.; Suzuki, Y.; Ouyang, Z.; Jiao, Z.; Shikazono, N. Operando observation of patterned nickel-gadolinium doped ceria solid oxide fuel cell anode. *J. Power Sources* **2021**, *516*, 230670.

(27) Liu, Y.; Wankmüller, F.; Lehnert, T. P.; Juckel, M.; Menzler, N. H.; Weber, A. Microstructural changes in nickel-ceria fuel electrodes at elevated temperature. *Fuel Cells* **2023**, *23*, 430−441.

(28) Chen, H.-Y.; Yu, H.-C.; Cronin, J. S.; Wilson, J. R.; Barnett, S. A.; Thornton, K. Simulation of coarsening in three-phase solid oxide fuel cell anodes. *J. Power Sources* **2011**, *196*, 1333−1337.

(29) Li, Q.; Liang, L.; Gerdes, K.; Chen, L.-Q. Phase-field modeling of three-phase electrode microstructures in solid oxide fuel cells. *Appl. Phys. Lett.* **2012**, *101*, 033909.

(30) Davis, R.; Abdeljawad, F.; Lillibridge, J.; Haataja, M. Phase wettability and microstructural evolution in solid oxide fuel cell anode materials. *Acta Mater.* **2014**, *78*, 271−281.

(31) Abdeljawad, F.; Völker, B.; Davis, R.; McMeeking, R. M.; Haataja, M. Connecting microstructural coarsening processes to electrochemical performance in solid oxide fuel cells: An integrated modeling approach. *J. Power Sources* **2014**, *250*, 319−331.

(32) Jiao, Z.; Shikazono, N. Prediction of nickel morphological evolution in composite solid oxide fuel cell anode using modified phase field model. *J. Electrochem. Soc.* **2018**, *165*, F55−F63.

(33) Lei, Y.; Cheng, T.-L.; Abernathy, H.; Epting, W.; Kalapos, T.; Hackett, G.; Wen, Y. Phase field simulation of anode microstructure evolution of solid oxide fuel cell through Ni (OH) 2 diffusion. *J. Power Sources* **2021**, *482*, 228971.

(34) Trini, M.; De Angelis, S.; Jørgensen, P. S.; Hendriksen, P. V.; Thornton, K.; Chen, M. Towards the validation of a phase field model for Ni coarsening in solid oxide cells. *Acta Mater.* **2021**, *212*, 116887.

(35) Lei, Y.; Lee, Y.-L.; Epting, W. K.; Mason, J. H.; Cheng, T.-L.; Abernathy, H.; Hackett, G.; Wen, Y.-H. Modeling Ni redistribution in

the hydrogen electrode of solid oxide cells through Ni(OH)$_2$ diffusion and Ni−YSZ. wettability change. *J. Power Sources* **2022**, *545*, 231924.

(36) Hoffrogge, P. W.; Schneider, D.; Wankmüller, F.; Meffert, M.; Gerthsen, D.; Weber, A.; Nestler, B.; Wieler, M. Performance estimation by multiphase-field simulations and transmission-line modeling of nickel coarsening in FIB-SEM reconstructed Ni−YSZ SOFC anodes I: Influence of wetting angle. *J. Power Sources* **2023**, *570*, 233031.

(37) Yang, S.; Gao, J.; Trini, M.; De Angelis, S.; Jørgensen, P. S.; Bowen, J. R.; Zhang, L.; Chen, M. Ni coarsening in Ni-yttria stabilized zirconia electrodes: Three-dimensional quantitative phase-field simulations supported by ex-situ ptychographic nano-tomography. *Acta Mater.* **2023**, *246*, 118708.

(38) Sun, M.; Li, A.; Zhang, X.; Fei, Y.; Zhu, L.; Huang, Z. Influence of operating conditions on the fuel electrode degradation of solid oxide electrolysis cell investigated by phase field model with wettability analysis. *J. Power Sources* **2023**, *587*, 233700.

(39) Lei, Y.; Mantz, Y. A.; Saidi, W. A.; Abernathy, H. W.; Wen, Y. Ni coarsening under humid atmosphere in the electrode of solid oxide cells: A combined study of density-functional theory and phase-field modeling. *J. Power Sources* **2024**, *613*, 234778.

(40) Sun, M.; Li, A.; Zhang, X.; Fei, Y.; Zhu, L.; Huang, Z. Microstructure Evolution and Performance Evaluation of Nickel/Gadolinium-Doped Ceria Fuel Electrode for Solid Oxide Fuel Cell Investigated by Integrated Meso-Scale Modeling, Preprint at SSRN, **2024**,

(41) Seol, D.; Hu, S.; Liu, Z.; Chen, L.; Kim, S.; Oh, K. Phase-field modeling of stress-induced surface instabilities in heteroepitaxial thin films. *J. Appl. Phys.* **2005**, *98*, 044910.

(42) Allen, S. M.; Cahn, J. W. A microscopic theory for antiphase boundary motion and its application to antiphase domain coarsening. *Acta Metall.* **1979**, *27*, 1085−1095.

(43) Cahn, J. W.; Hilliard, J. E. Free energy of a nonuniform system. I. Interfacial free energy. *J. Chem. Phys.* **1958**, *28*, 258−267.

(44) Lei, Y.; Cheng, T.-L.; Wen, Y.-H. Phase field modeling of microstructure evolution and concomitant effective conductivity change in solid oxide fuel cell electrodes. *J. Power Sources* **2017**, *345*, 275−289.

(45) Chen, L.-Q.; Fan, D. Computer Simulation Model for Coupled Grain Growth and Ostwald Ripening—Application to Al2O3-ZrO2 Two-Phase Systems. *J. Am. Ceram. Soc.* **1996**, *79*, 1163−1168.

(46) Choudhury, A.; Nestler, B. Grand-potential formulation for multicomponent phase transformations combined with thin-interface asymptotics of the double-obstacle potential. *Phys. Rev. E:Stat., Nonlinear, Soft Matter Phys.* **2012**, *85*, 021602.

(47) Hoffrogge, P. W.; Mukherjee, A.; Nani, E.; Amos, P. K.; Wang, F.; Schneider, D.; Nestler, B. Multiphase-field model for surface diffusion and attachment kinetics in the grand-potential framework. *Phys. Rev. E* **2021**, *103*, 033307.

(48) Jeela, R. K.; Tosato, G.; Ahmad, M.; Wieler, M.; Koeppe, A.; Nestler, B.; Schneider, D. Enhancing Solid Oxide Fuel Cells Development through Bayesian Active Learning. *Adv. Energy Mater.* **2025**, *15*, 2501216.

(49) Klotz, D.; Weber, A.; Ivers-Tiffée, E. Practical guidelines for reliable electrochemical characterization of solid oxide fuel cells. *Electrochim. Acta* **2017**, *227*, 110−126.

(50) Irshad, M.; Siraj, K.; Raza, R.; Ali, A.; Tiwari, P.; Zhu, B.; Rafique, A.; Ali, A.; Kaleem Ullah, M.; Usman, A. A brief description of high temperature solid oxide fuel cell's operation, materials, design, fabrication technologies and performance. *Appl. Sci.* **2016**, *6*, 75.

(51) Blakely, J.; Mykura, H. Surface self diffusion measurements on nickel by the mass transfer method. *Acta Metall.* **1961**, *9*, 23−31.

(52) Nestler, B.; Garcke, H.; Stinner, B. Multicomponent alloy solidification: phase-field modeling and simulations. *Phys. Rev. E: Stat., Nonlinear, Soft Matter Phys.* **2005**, *71*, 041609.

(53) Steinbach, I.; Pezzolla, F. A. generalized field method for multiphase transformations using interface fields. *Phys. D* **1999**, *134*, 385−393.

(54) Hoffrogge, P.; Daubner, S.; Schneider, D.; Nestler, B.; Zhou, B.; Eiken, J. Triple junction benchmark for multiphase-field models combining capillary and bulk driving forces. *Modell. Simul. Mater. Sci. Eng.* **2025**, *33*, 015001.

(55) Seiz, M.; Hoffrogge, P.; Hierl, H.; Reiter, A.; Schneider, D.; Nestler, B. Phase-Field Simulations with the Grand Potential Approach. In *High Performance Computing in Science and Engineering'20: Transactions of the High Performance Computing Center, Stuttgart (HLRS) 2020*; Springer: Stuttgart, Germany, 2022; pp 561−577.

(56) Sun, Y.; Beckermann, C. Sharp interface tracking using the phase-field equation. *J. Comput. Phys.* **2007**, *220*, 626−653.

(57) Hayward, E.; Greenough, A. The surface energy of solid nickel. *J. Inst. Met.* **1959**, *88*, 217−220.

(58) Maiya, P.; Blakely, J. Surface self-diffusion and surface energy of nickel. *J. Appl. Phys.* **1967**, *38*, 698−704.

(59) Clark, E.; Yeske, R.; Birnbaum, H. The effect of hydrogen on the surface energy of nickel. *Metall. Trans. A* **1980**, *11*, 1903−1908.

(60) Murr, L.; Inal, O.; Wong, G. Applications of the SEM, TEM, and FIM in the analysis of structure and energy of metal interfaces. In *Electron microscopy and structure of materials*; University of California Press: Berkeley, 1972; pp 417−426.

(61) Symington, A. R.; Molinari, M.; Moxon, S.; Flitcroft, J. M.; Sayle, D. C.; Parker, S. C. Strongly bound surface water affects the shape evolution of cerium oxide nanoparticles. *J. Phys. Chem. C* **2020**, *124*, 3577−3588.

(62) Zouvelou, N.; Mantzouris, X.; Nikolopoulos, P. Surface and grain-boundary energies as well as surface mass transport in polycrystalline CeO$_2$. *Mater. Sci. Eng., A* **2008**, *495*, 54−59.

(63) Münch, B.; Holzer, L. Contradicting geometrical concepts in pore size analysis attained with electron microscopy and mercury intrusion. *J. Am. Ceram. Soc.* **2008**, *91*, 4059−4067.

(64) Joos, J.; Carraro, T.; Weber, A.; Ivers-Tiffée, E. Reconstruction of porous electrodes by FIB/SEM for detailed microstructure modeling. *J. Power Sources* **2011**, *196*, 7302−7307.

(65) Palágyi, K.; Kuba, A. A 3D 6-subiteration thinning algorithm for extracting medial lines. *Pattern Recognit. Lett.* **1998**, *19*, 613−627.

(66) Nakamura, T.; Kobayashi, T.; Yashiro, K.; Kaimai, A.; Otake, T.; Sato, K.; Mizusaki, J.; Kawada, T. Electrochemical behaviors of mixed conducting oxide anodes for solid oxide fuel cell. *J. Electrochem. Soc.* **2008**, *155*, B563−B569.

(67) Joos, J. *Microstructural Characterisation, Modelling and Simulation of Solid Oxide Fuel Cell Cathodes*; KIT Scientific Publishing, 2017; Vol. *30*.

(68) Sciazko, A.; Komatsu, Y.; Shimura, T.; Shikazono, N. Multiscale microstructural evolutions of nickel-gadolinium doped ceria in solid oxide fuel cell anode. *J. Power Sources* **2020**, *478*, 228710.

(69) Jiao, Z.; Busso, E. P.; Shikazono, N. Influence of polarization on the morphological changes of nickel in fuel electrodes of solid oxide cells. *J. Electrochem. Soc.* **2020**, *167*, 024516.

(70) Ihara, S.; Naruse, S.; Muroyama, H.; Matsui, T. Wettability analysis of Ni/YSZ interface under operating conditions of solid oxide cells. *J. Power Sources* **2025**, *654*, 237867.